Mechanics of Star Formation

Frank Shu

University of California, Berkeley
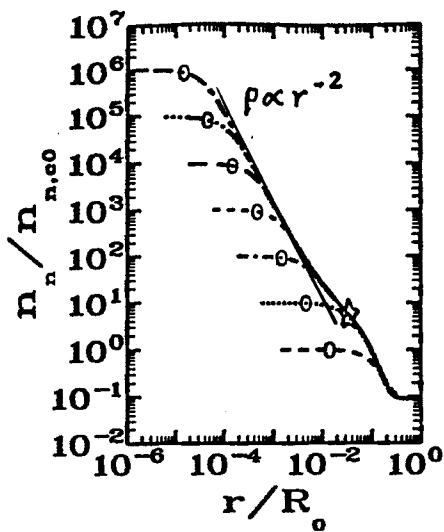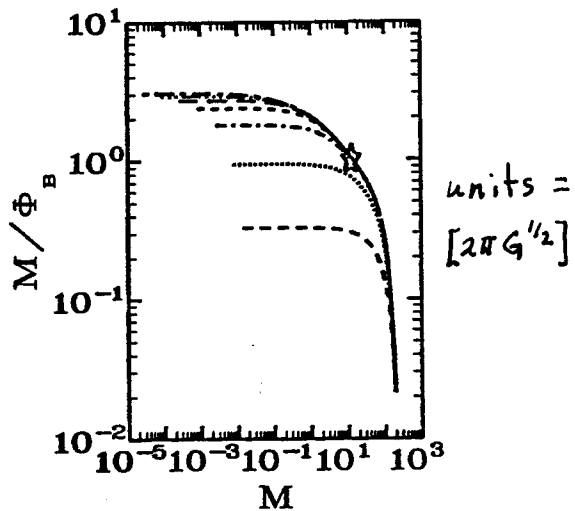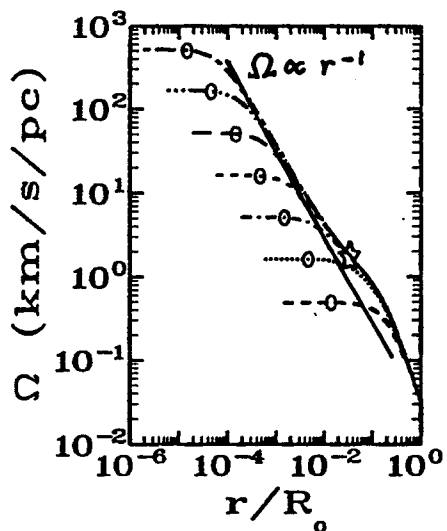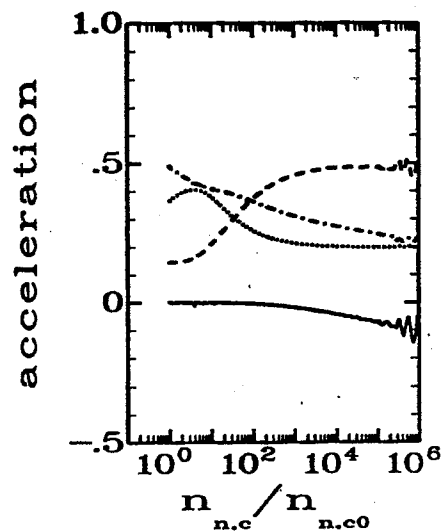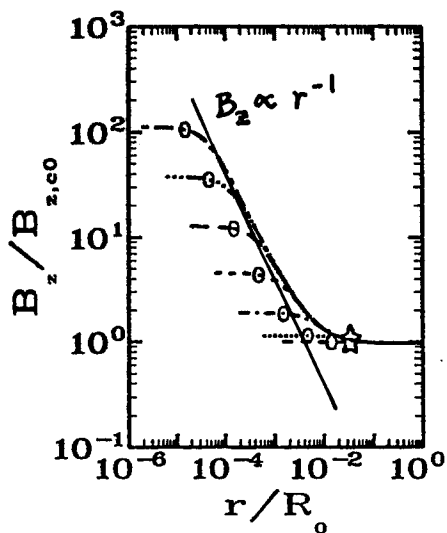
Basu & Mouschovias (1994)

Fig. 3a
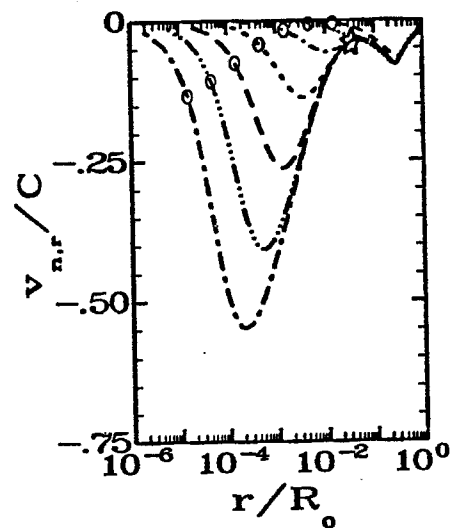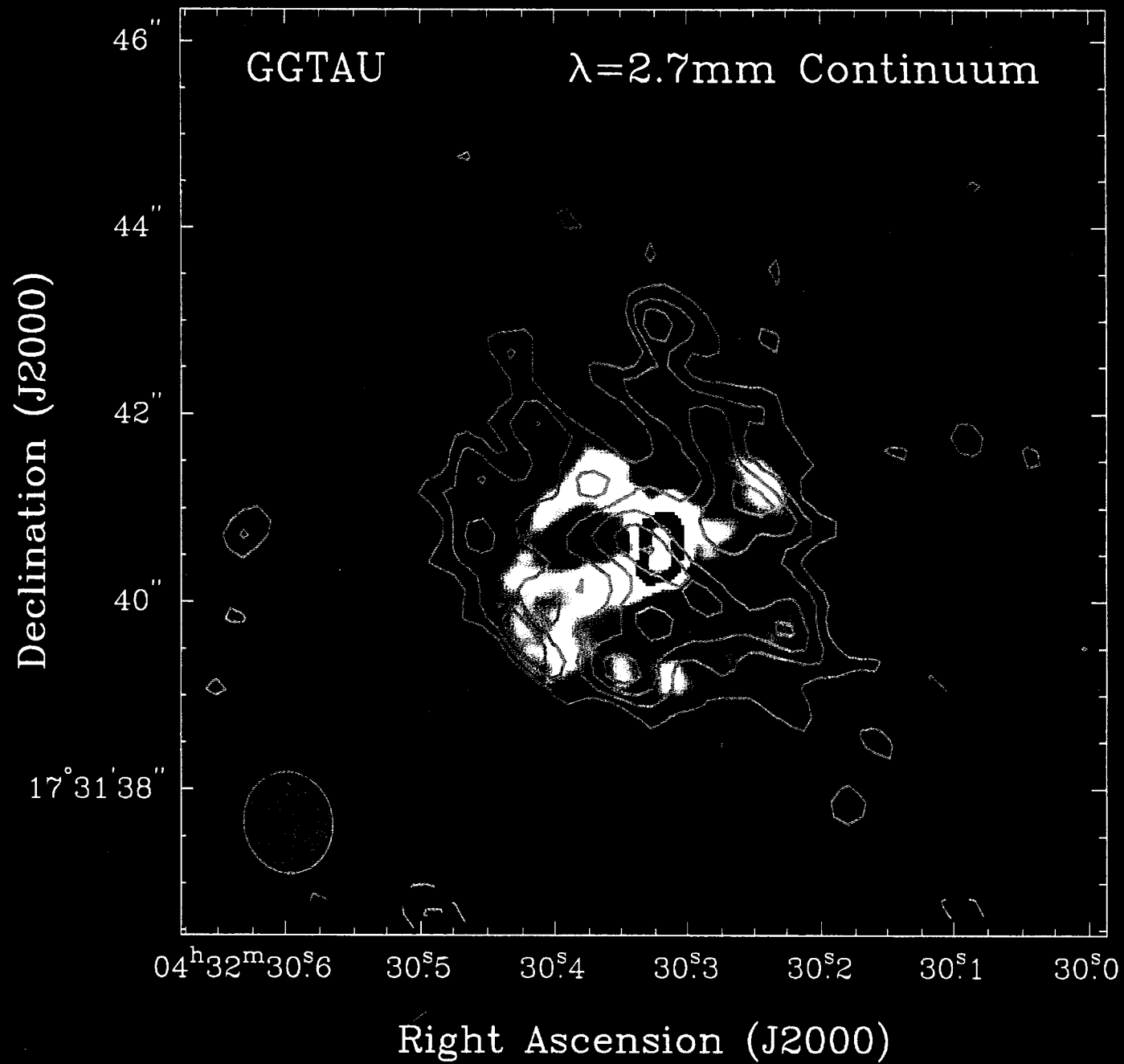
TWO EXTREME POSSIBILITIES

1) All clouds are magnetically subcritical:

a) Increase M relative to M_Φ, e.g.,

double M, same $\overline{\Phi}$
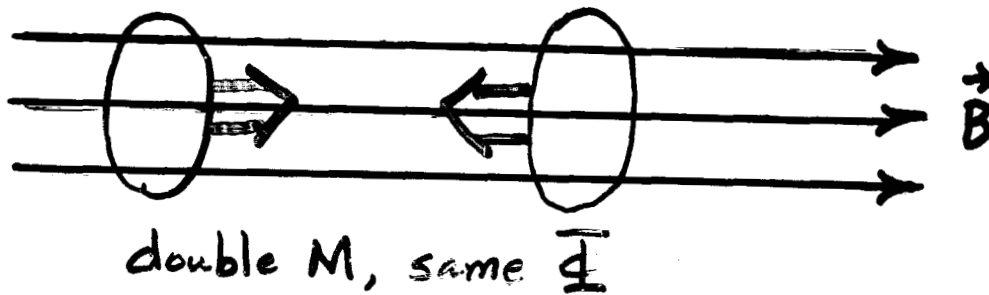
Clustered mode?

b) Decrease M_Φ relative to M by ambipolar diffusion:
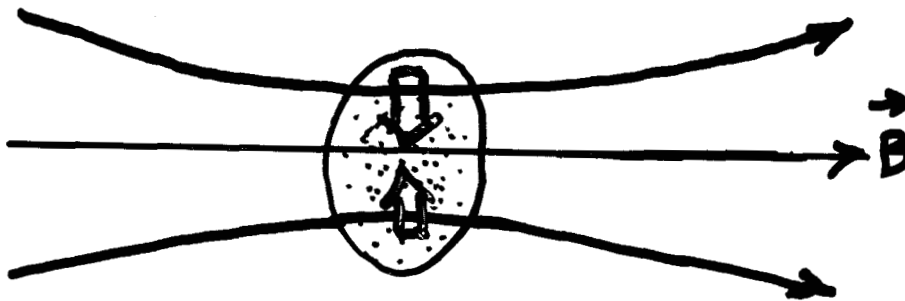
Isolated mode?

2) All clouds are magnetically supercritical:

a) Wait for tubulence to decay

b) Feedback necessary if not to have too high a rate of star formation (strong constraint only in distributed mode?)

MAGNETIC SUPPORT OF MAGNETIC CLOUDS

(Mestel & Spitzer 1956, Mestel 1965, Strittmatter 1966)

Magnetic Critical Mass:

$$M_\Phi \equiv \frac{\Phi}{2\pi G^{1/2}}.$$

Isothermal Sound Speed:

$$a \equiv \left(\frac{kT}{m}\right)^{1/2}.$$

External Pressure Needed to Confine Cloud of Mass M Threaded by Magnetic Flux Φ to Volume V (Virial Theorem):

$$P_{\text{ext}} = \frac{Ma^2}{V} + \frac{\alpha G}{V^{4/3}}\left(M_\Phi^2 - M^2\right).$$

$M \gtrsim M_\Phi$

Can collapse but not fragment unless highly flattened
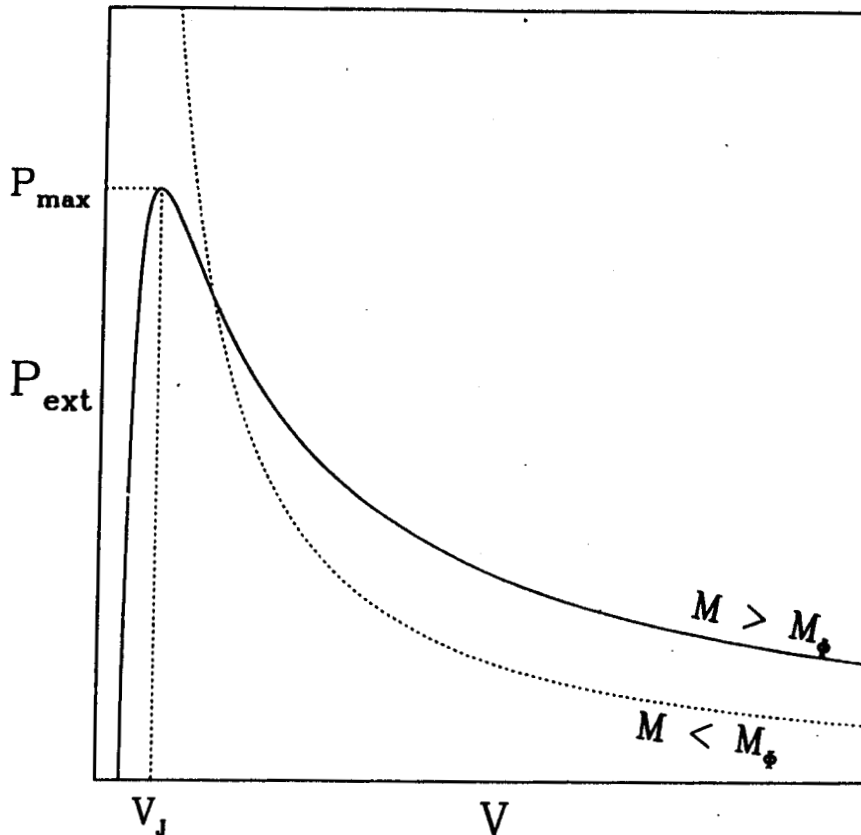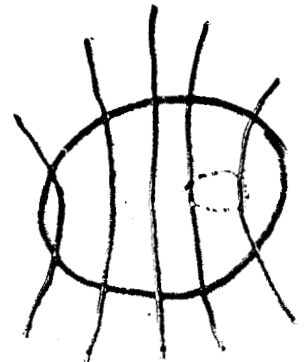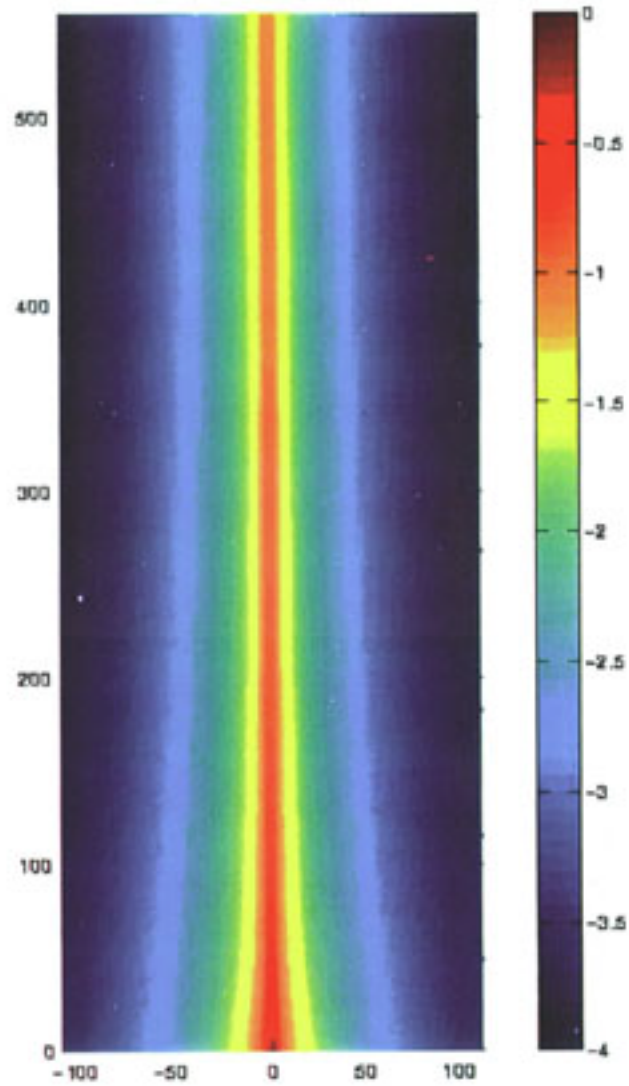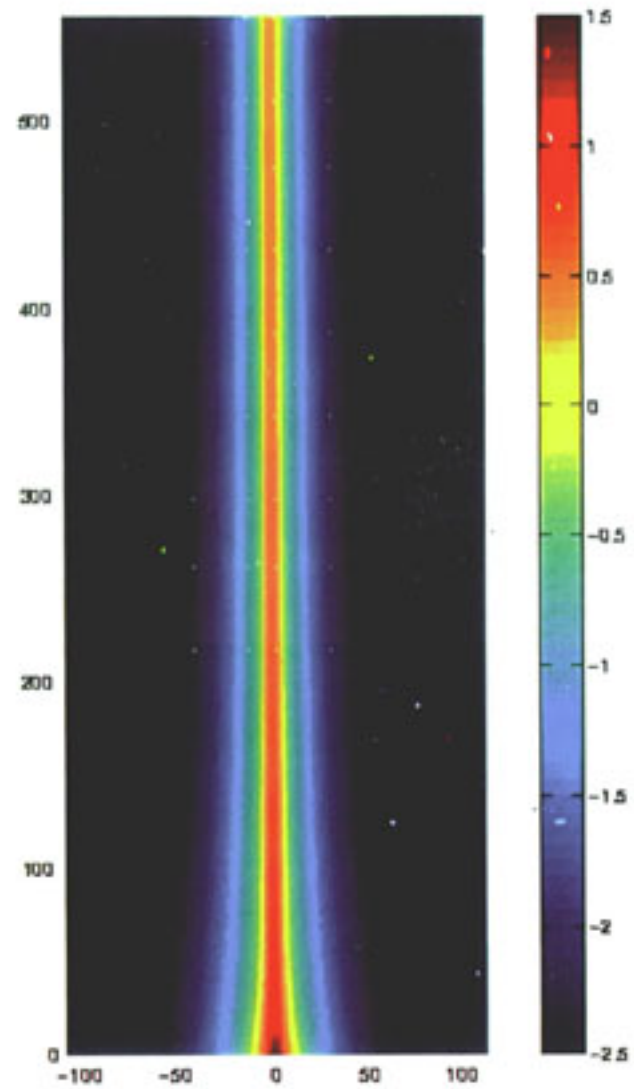
TABLE 1. Zeeman Measurements from Crutcher (1999)

Cloud	$N(H_2)$ (10^{22} cm^{-2})	$B_\parallel$ (μG)	$mN(H_2)/B_\parallel$ $(2\pi G^{1/2})^{-1}$	$\Sigma/B \equiv \lambda$ $(2\pi G^{1/2})^{-1}$
W3OH	50.1	3100	1.1	0.3
DR21OH1	39.8	710	3.6	0.9
SgrB2	25.1	480	3.4	0.9
M17SW	12.6	450	1.8	0.5
W3	15.8	400	2.6	0.6
S106	6.3	400	1.0	0.3
DR21OH2	20.0	360	3.6	0.9
OMC1	15.8	360	2.9	0.7
NGC2024	7.9	87	5.9	1.5
S88B	2.0	69	1.9	0.5
B1	0.8	27	1.9	0.5
W49B	0.4	21	1.2	0.3
W22	1.6	18	5.7	1.4
W40	1.0	14	4.6	1.2
ρ Oph1	0.5	10	3.3	0.8
OMCN4	12.6	<280	> 2.9	> 0.7
TauG	0.4	<16	> 1.6	> 0.4
L183	0.2	<16	> 0.6	> 0.2
L1647	1.3	<15	> 5.5	> 1.4
ρ Oph2	0.4	<14	> 1.8	> 0.5
TMC1	0.8	<13	> 4.0	> 1.0
L1495W	0.4	<13	> 2.0	> 0.5
L134	0.2	<11	> 1.2	> 0.3
TMC1C	0.8	<9	> 5.7	> 1.4
L1521	0.5	<9	> 3.6	> 0.9
L889	1.0	<7	> 9.3	> 2.3
Tau16	0.5	<7	> 4.7	> 1.2

SII

OI

Shang, Shu & Glassgold (1998)

Shu, Najita, Ostriker, Wilkin, Ruden, & Lizano (1994)

critical
equipotential

Alfven surface

super-Alfvenic
flow

critical
equipotential

dead zone
coronal gas
soft x-rays

x-wind

uv hot spot
ultraviolet
excess

star

funnel
flow

force-free
field

sub-Alfvenic
flow

disk

infrared excess

R_*

R_x

sonic
surface

sonic
surface

$\dot{M}_W = \frac{1}{3}\dot{M}_0$

$f = \frac{1-\bar{J}_x-\tau}{\bar{J}_W-\bar{J}_x} \approx \frac{1}{3}$

$V_W(\infty) = \sqrt{2\bar{J}_W-3}\,R_x\Omega$

$R_x = \bar{\Phi}_{dx}^{-4/7}\left(\frac{\beta_*^4}{GM_*\dot{M}_0^2}\right)^{1/7}$

$2\bar{\beta}_W f^{1/2} \approx \frac{2}{\sqrt{3}} = 1.15$

Steady State : $\Omega_* = \Omega_x = \left(\frac{GM_*}{R_x^3}\right)^{1/2}$

Fig
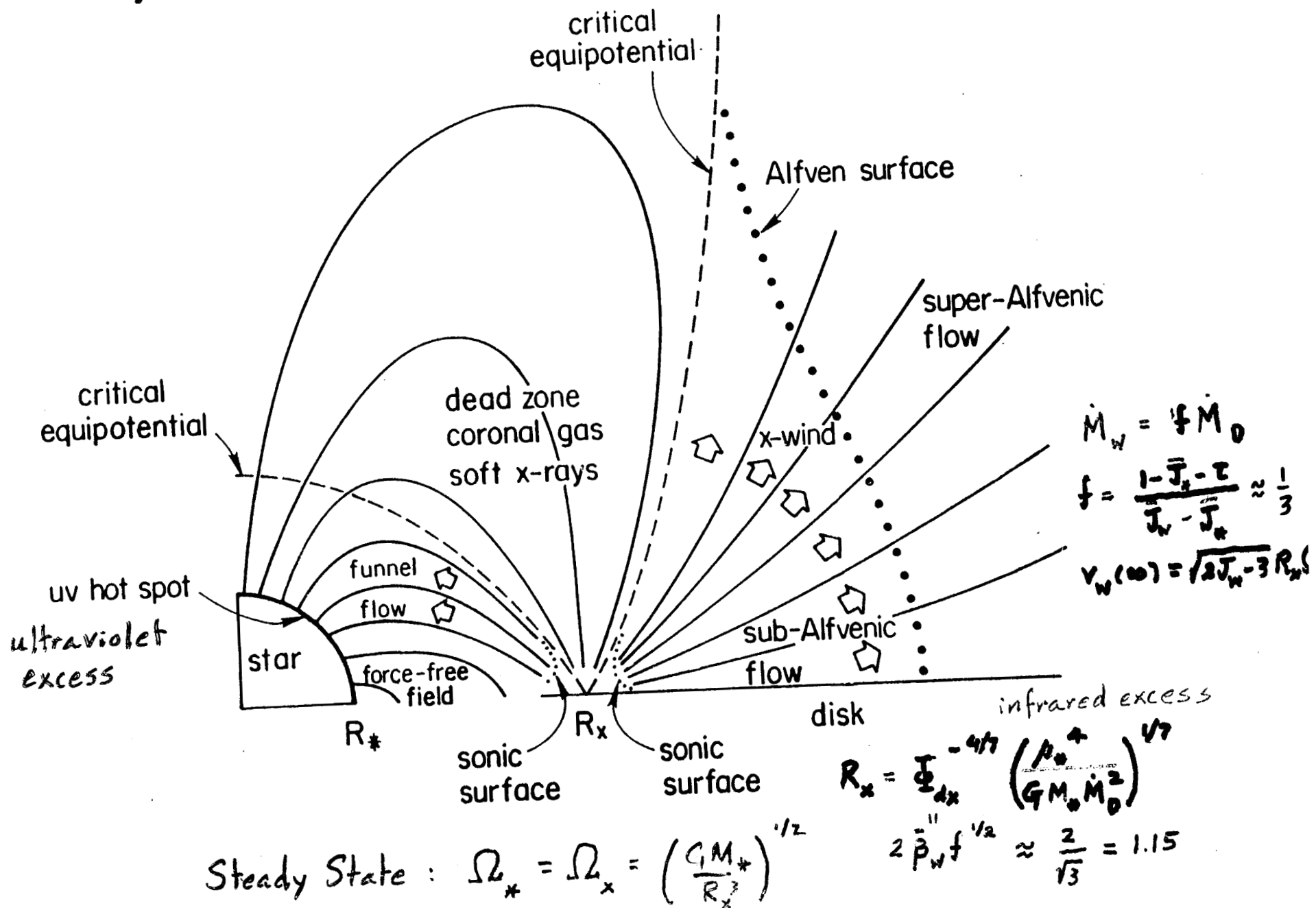
Diagram of HH 30 Circumstellar Disk & Jet

Proto-Star

Accretion Disk—

——Jet

No! Optical illusion.

HH30

HH34

HH47
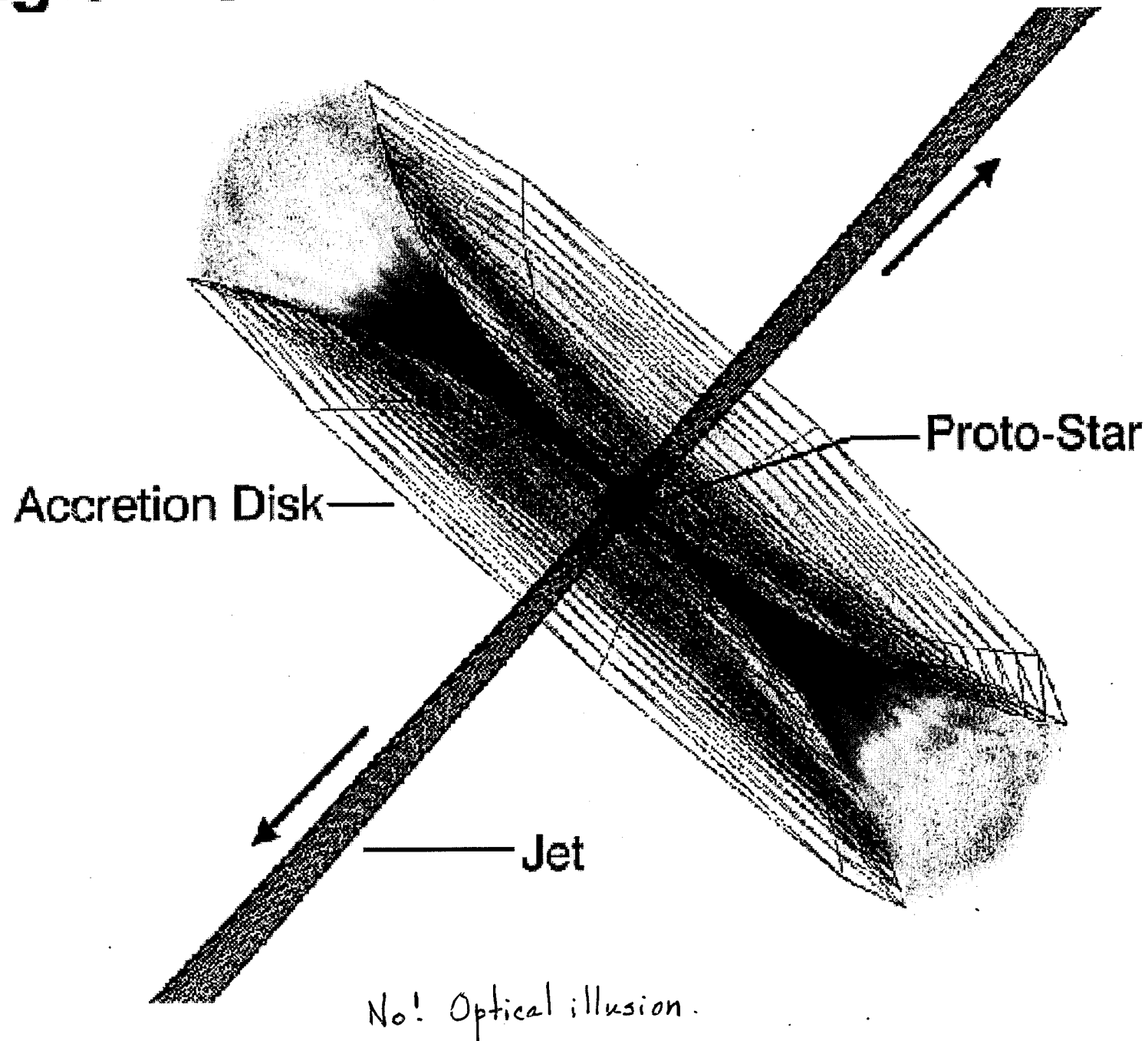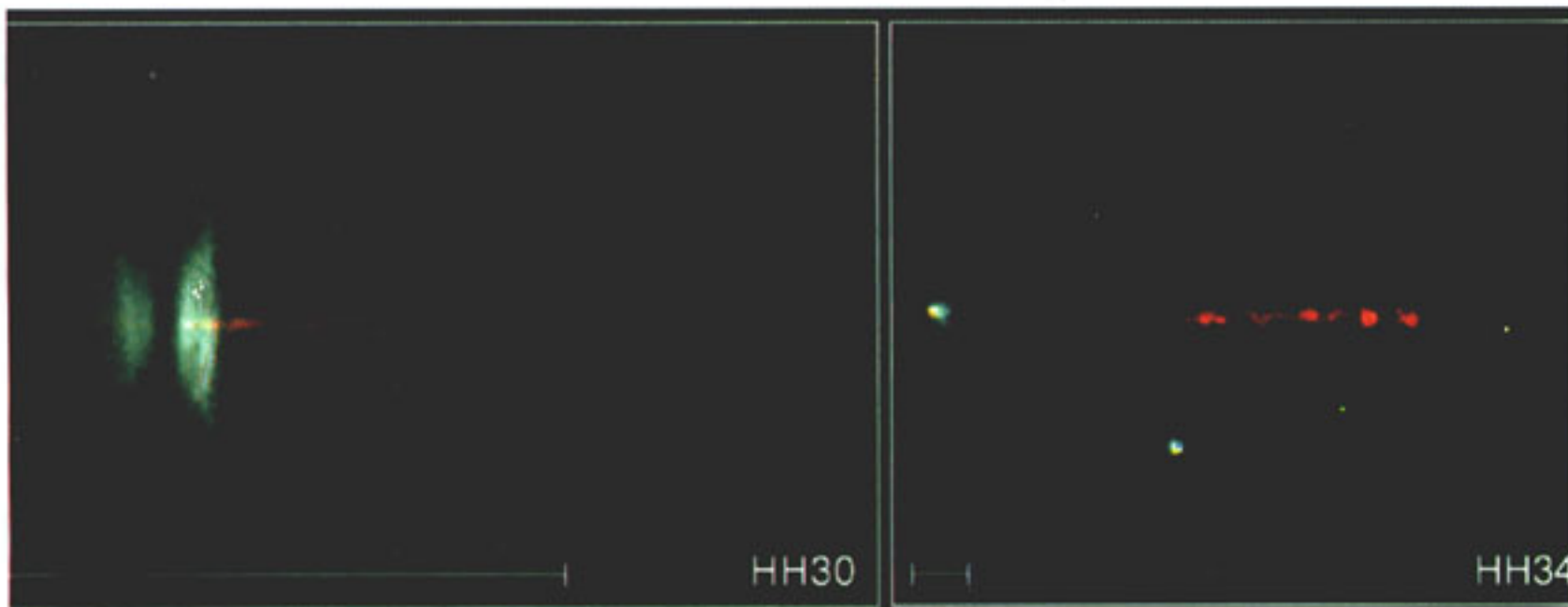
Jets from Young Stars

HST · WFPC2

FIG. 10.—Evolutionary tracks in the H-R diagram for all computed masses. We also include the tracks for $M_* = 0.6\ M_\odot$ and $1.0\ M_\odot$, as obtained by Parig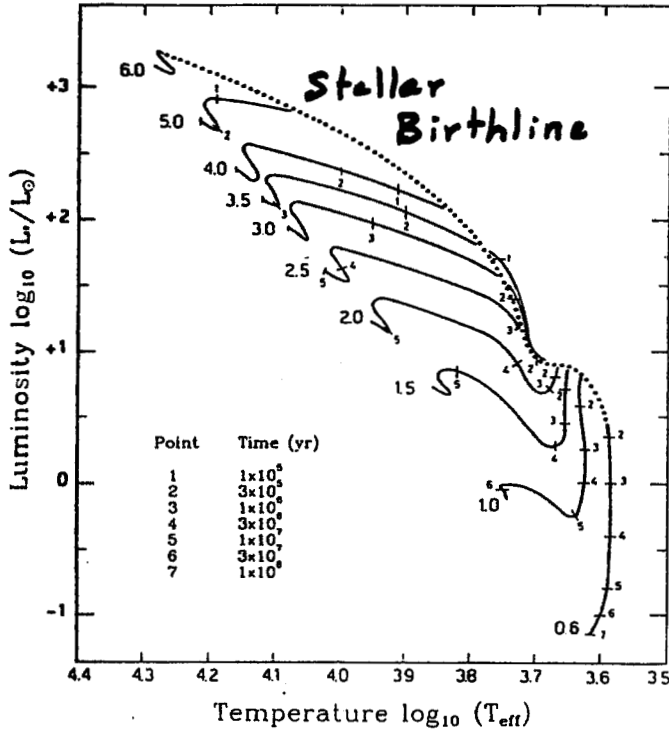i (1992). Each track is labeled by the corresponding mass in solar units. Tick marks indicate evolutionary times, as given in the table. Each track starts at the birthline (*dotted curve*) and ends at the ZAMS. The latter curve has been omitted for clarity.
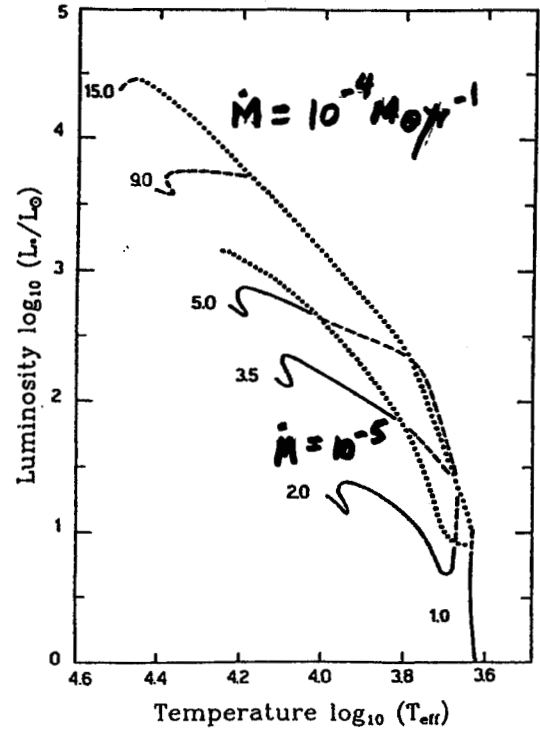
FIG. 12.—Effect of the protostellar mass accretion rate on pre–main-sequence evolution in the H-R diagram. The tracks of selected masses are shown schematically (*dashed curves*), starting from the birthline computed with $\dot{M} = 10^{-4}\ M_\odot\ \mathrm{yr}^{-1}$ (*open circles*). Stars of lower mass join onto standard tracks (*solid curves*) by the time they have crossed the birthline corresponding to $\dot{M} = 10^{-5}\ M_\odot\ \mathrm{yr}^{-1}$ (*dotted curve*). The displayed portions of the 9 and 15 $M_\odot$ tracks are from Iben (1965).

In spherical theory, cutoff after Δt_* of $\dot{M} = $ const is arbitrary; otherwise, no way to define

$$M_* = \dot{M}\,\Delta t_*$$

For sunlike stars, confirm validity of Hayashi pre-main-seq. tracks; locus of stellar birthline largely set by steady deuterium burning in protostellar phase ($\dot{M}$ const)
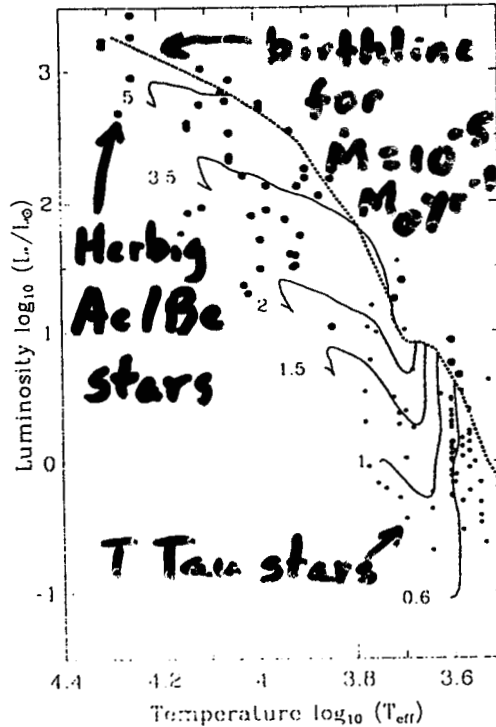
FIG. 13.—Observed distribution of low- and intermediate-mass pre–main-sequence stars in the H-R diagram. Data for Herbig Ae/Be stars (*large filled circles*) are taken from Berrilli et al. (1992), while the T Tauri stars (*small dots*) are from Strom et al. (1989). The theoretical tracks and birthline are the same as in Fig. 10.

MECHANICS OF STAR FORMATION

Frank H. Shu

University of California at Berkeley

Outline of Lecture

- Four Stages of the Formation of Sunlike Stars

    1. Condensation of Molecular Cloud Cores

    2. Gravitational Collapse and Protostars

    3. Winds, Jets, and Bipolar Outflows

    4. T Tauri Stars and Protoplanetary Disks

- Some Big Open Issues

    1. Distinction Between Single and Multiple Star Formation

    2. Distinction Between Low-Mass and High-Mass Star Formation

    3. Distributed versus Clustered Star Formation

    4. What Determines the Initial Mass Function?

    5. What Sets the Rate of Star Formation in GMCs? In Galaxies?

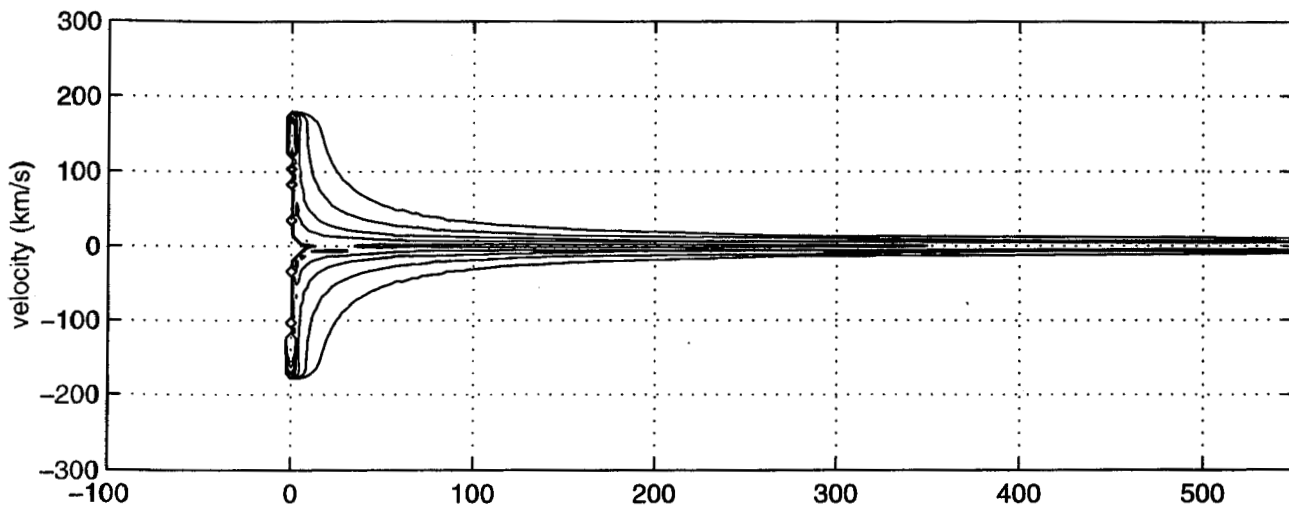   6. How Common is Planet Formation? Do Disks = Planets?

References

The Origin of Stars and Planetary Systems, 1999, ed. C. J. Lada & N. D. Kylafis (Dirdrecht: Kluwer)
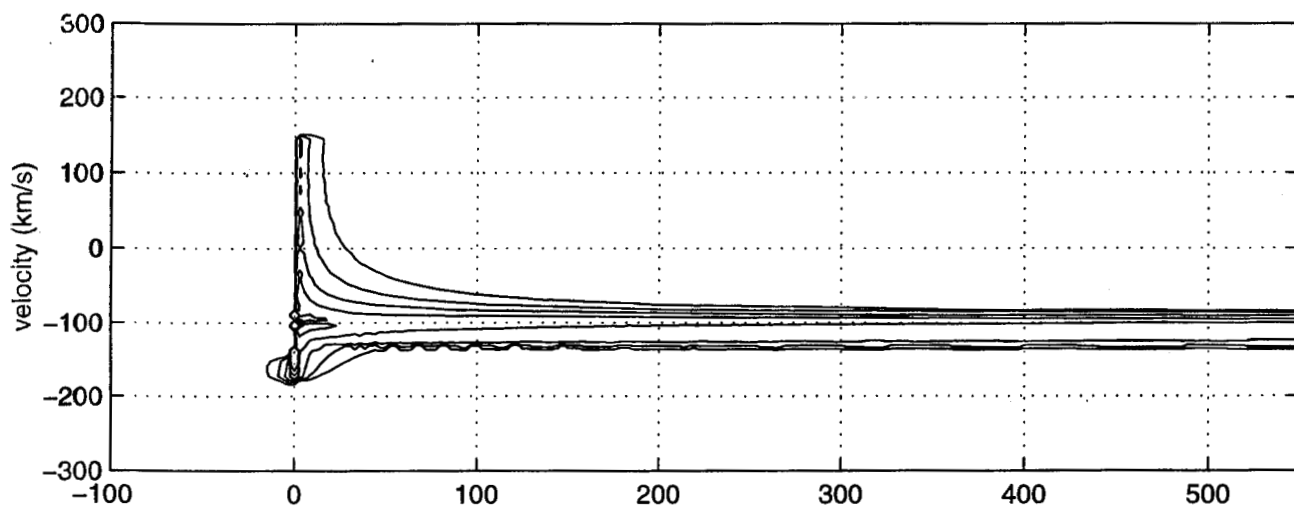
Protostars and Planets IV, 2000, ed. V. Mannings, A. P. Boss, & S. S. Russell (Tucson: University of Arizona Press)

O'Dell (1999)

Shang, Shu, Glassgold (1998)

$i = 40°$

$i = 60°$

$i = 30°$
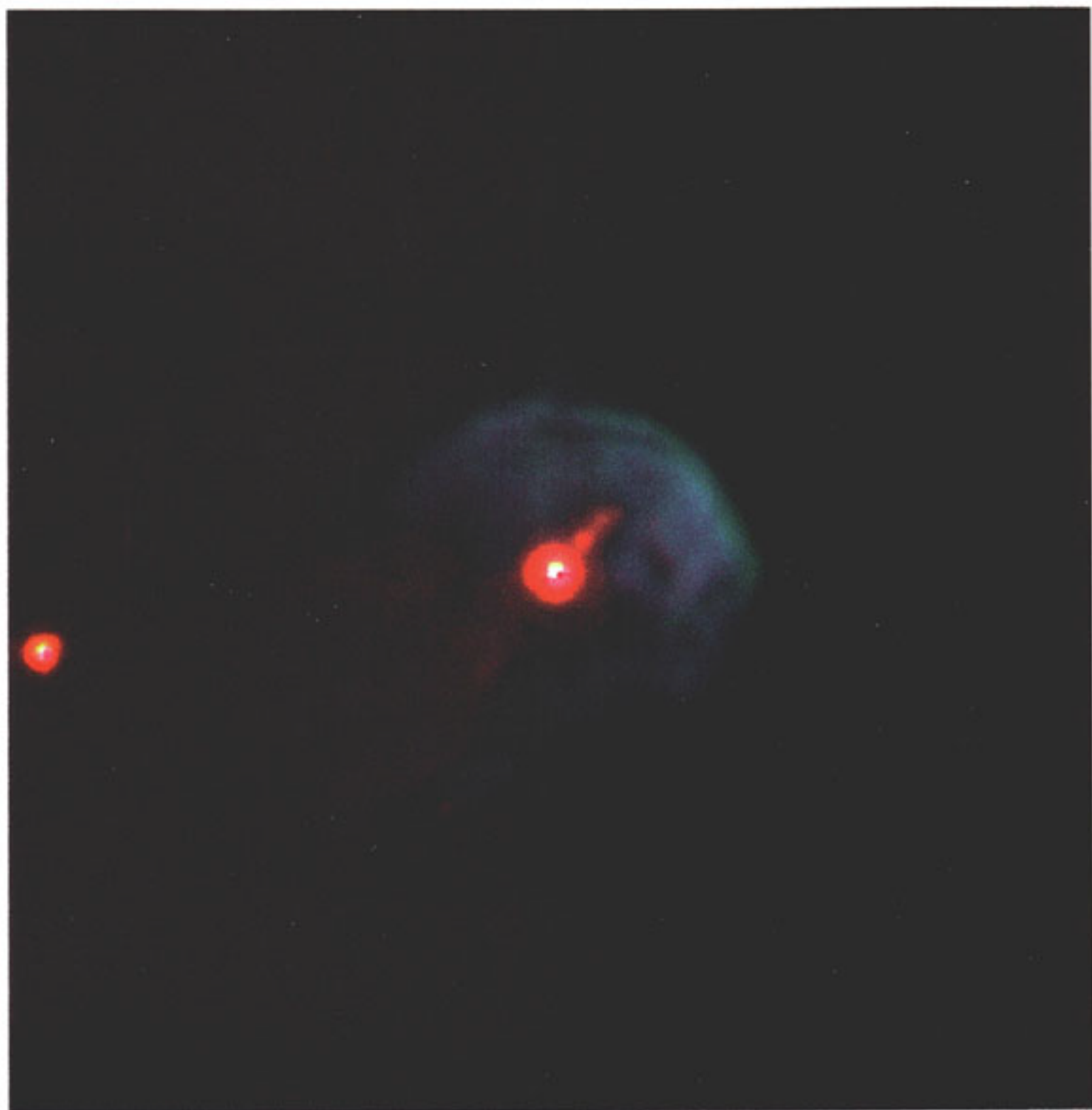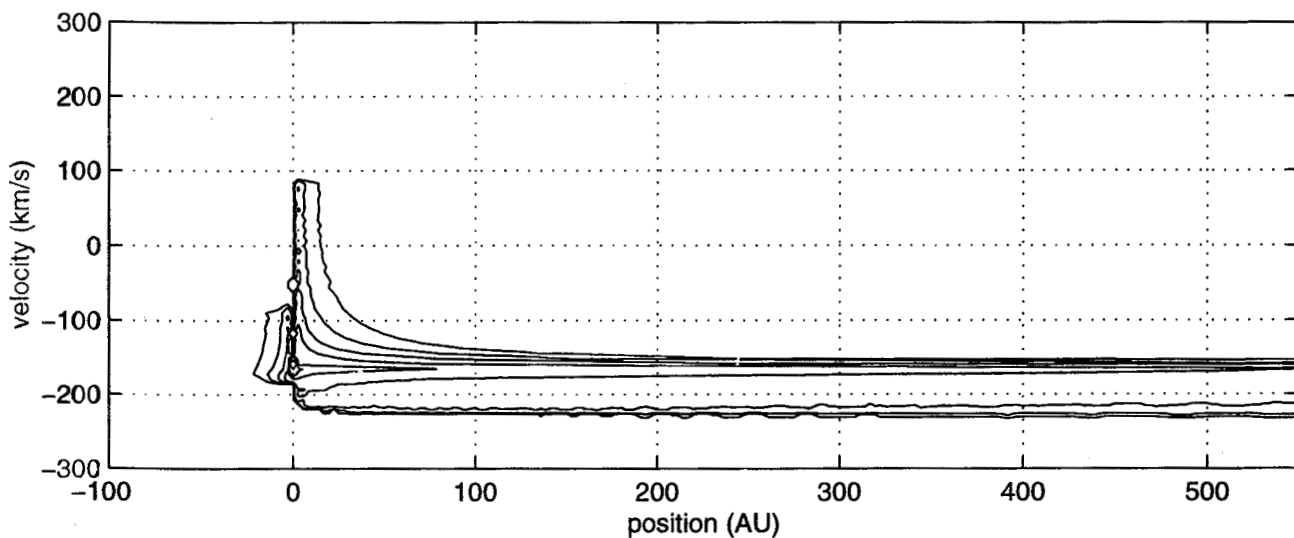
Bacciotti, Chiuderi, + Oliva (1995)
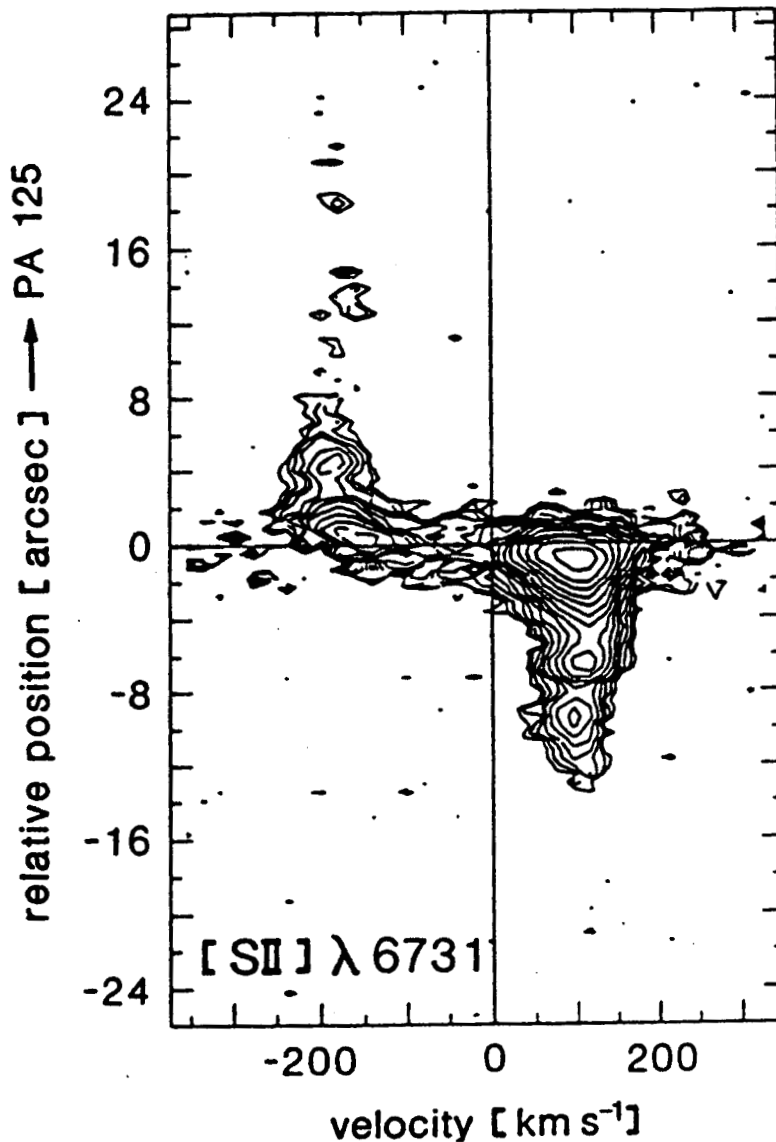
Fig. 1. Position-velocity map of the [SII]λ 6731 line in the bipolar outflow of RW Aurigae

fading?

$n_e \sim 10^4 cm^{-3}$

$\alpha \sim 10^{-13} cm^3 s^{-1}$

$t_{rec} \sim \frac{1}{\alpha \cdot n_e} \sim 10^9 s$

$L \sim v_w t_{rec} \sim 3 \times 10^{16} cm$

What provides heating and (initial) ionization?
Speculation: Protostellar X-rays. (quasi FGH theory)

[O I] 6300Å

Orion nebula

Microjet

Proplyd

Countermicrojet

5 "

Geocoronal
emission

244-440

slit position (pixels)

Heliocentric velocity (km/s)
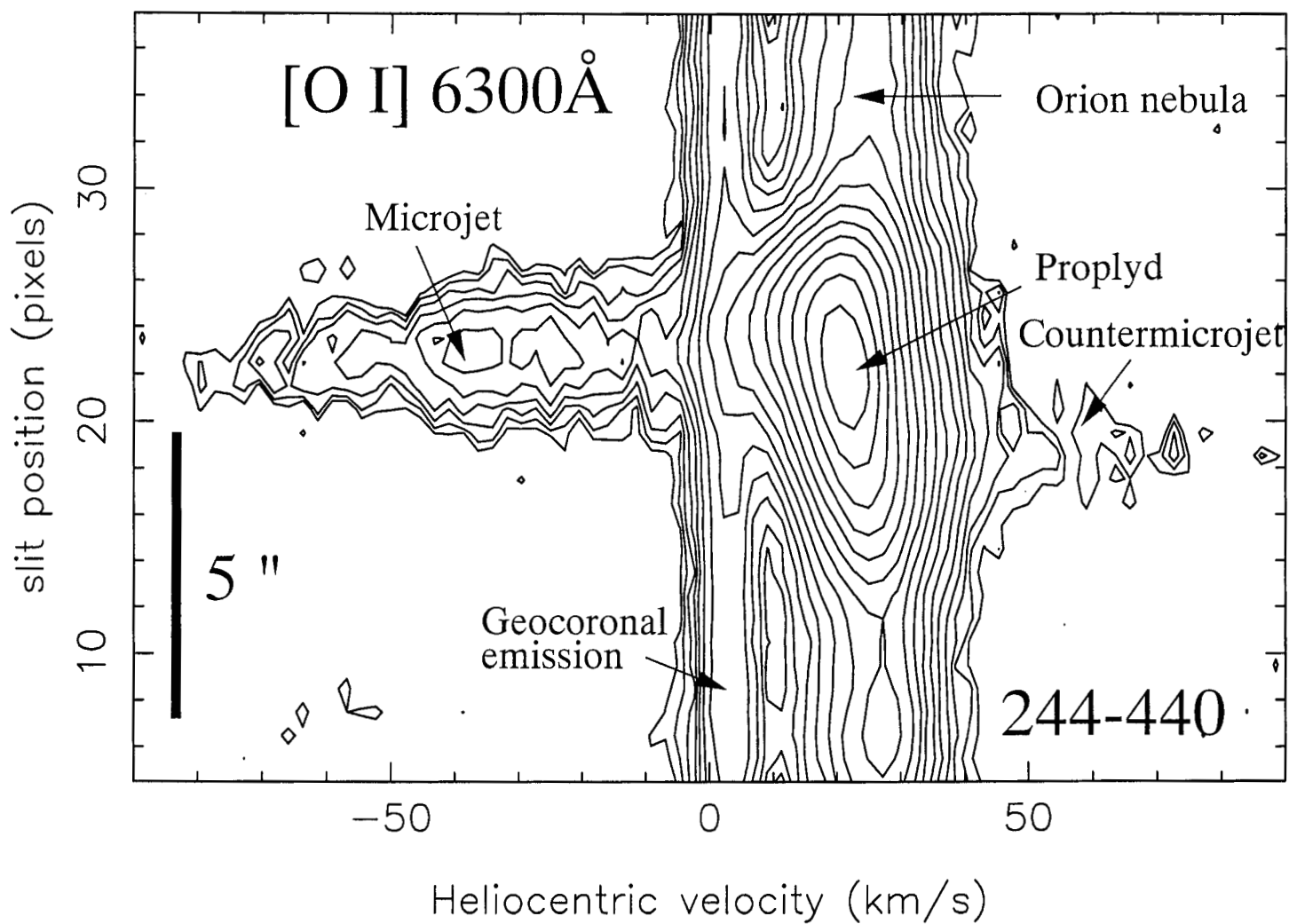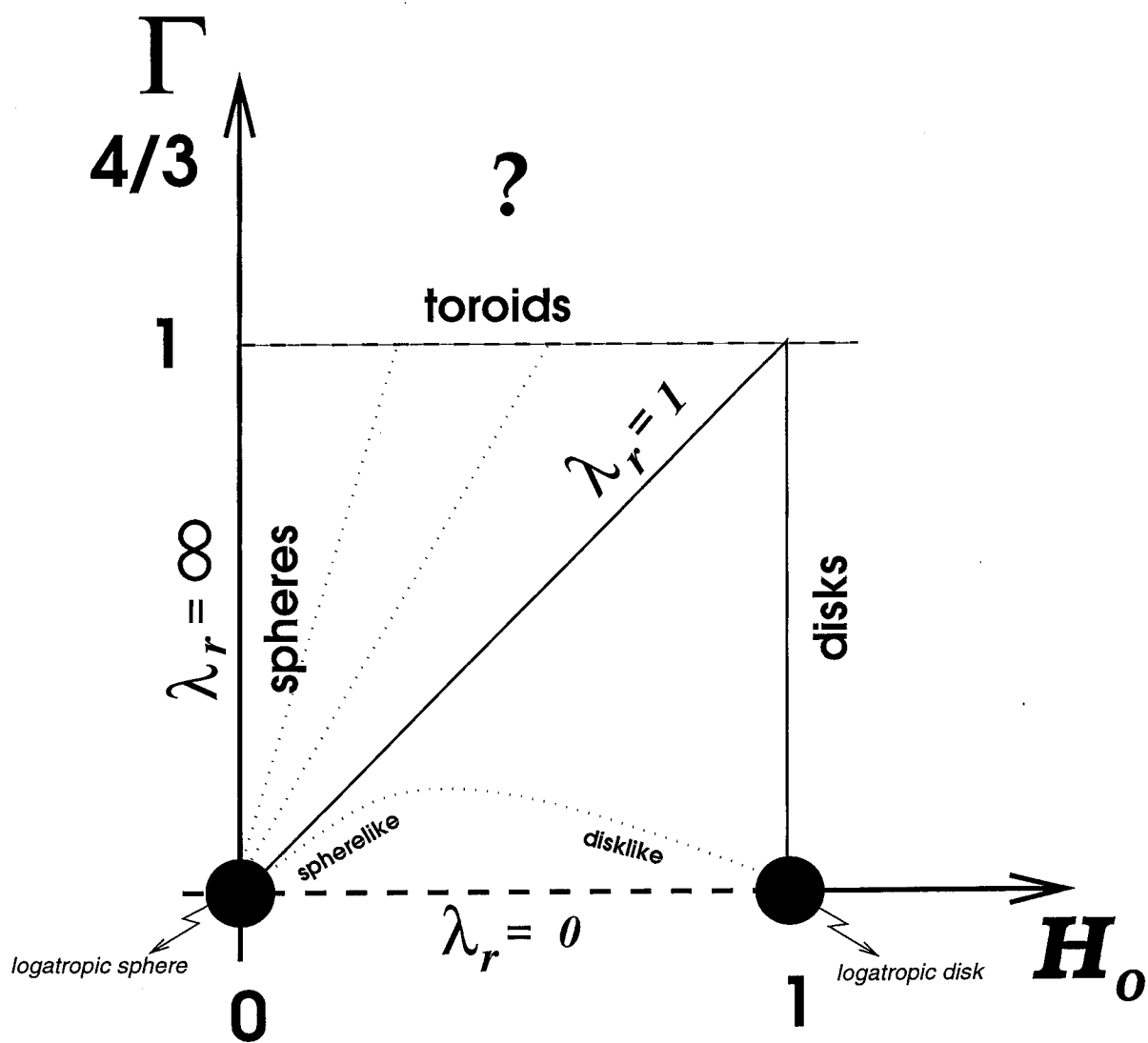
HH 34 _____ 60" _____
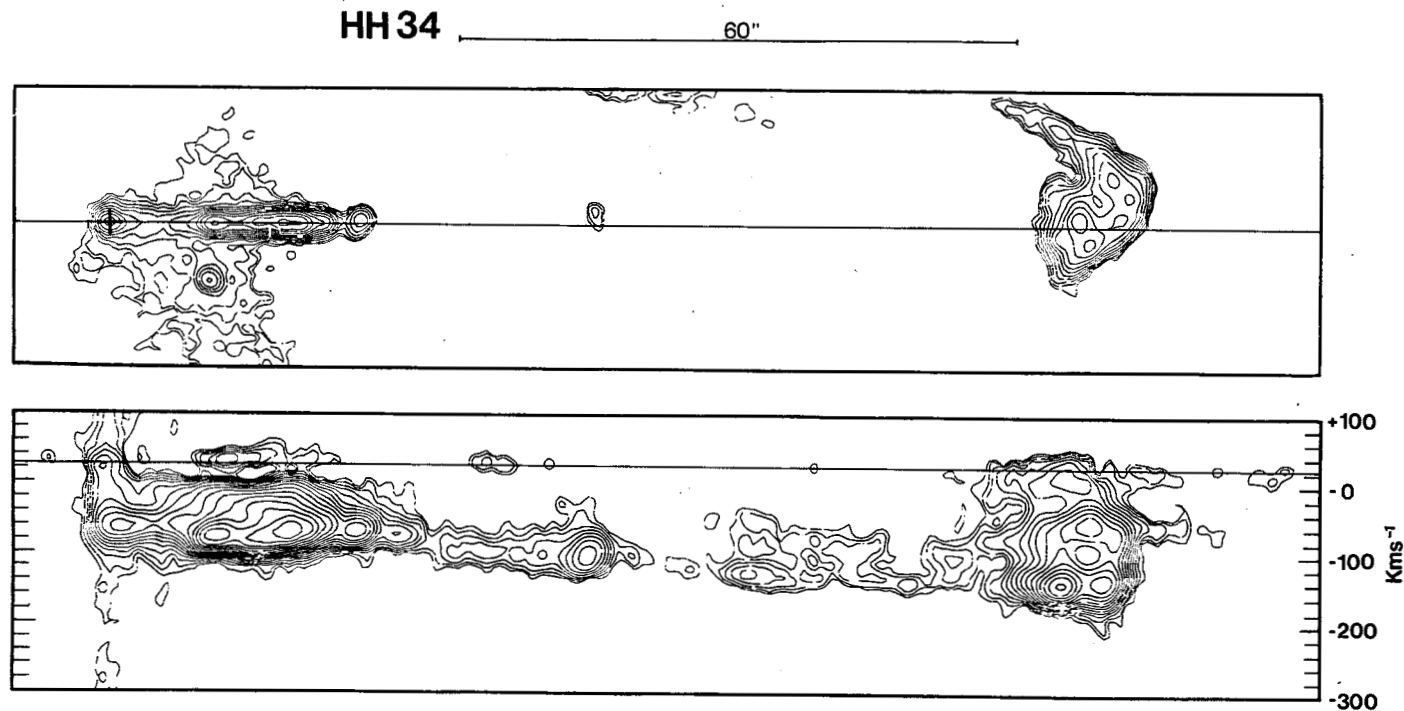
Figure 16. A direct image and an echelle spectrum of the HH 34 flow, shown as contour plots, on the same scale. The line through the direct image shows the slit position. The long slit spectrum is the sum of the [SII] 6717/6731 lines, showing the blueshifted jet emission. The position of sky emission, which has been carefully subtracted, is indicated by a line. Further details are given in the text. From Heathcote and Reipurth (1990c).
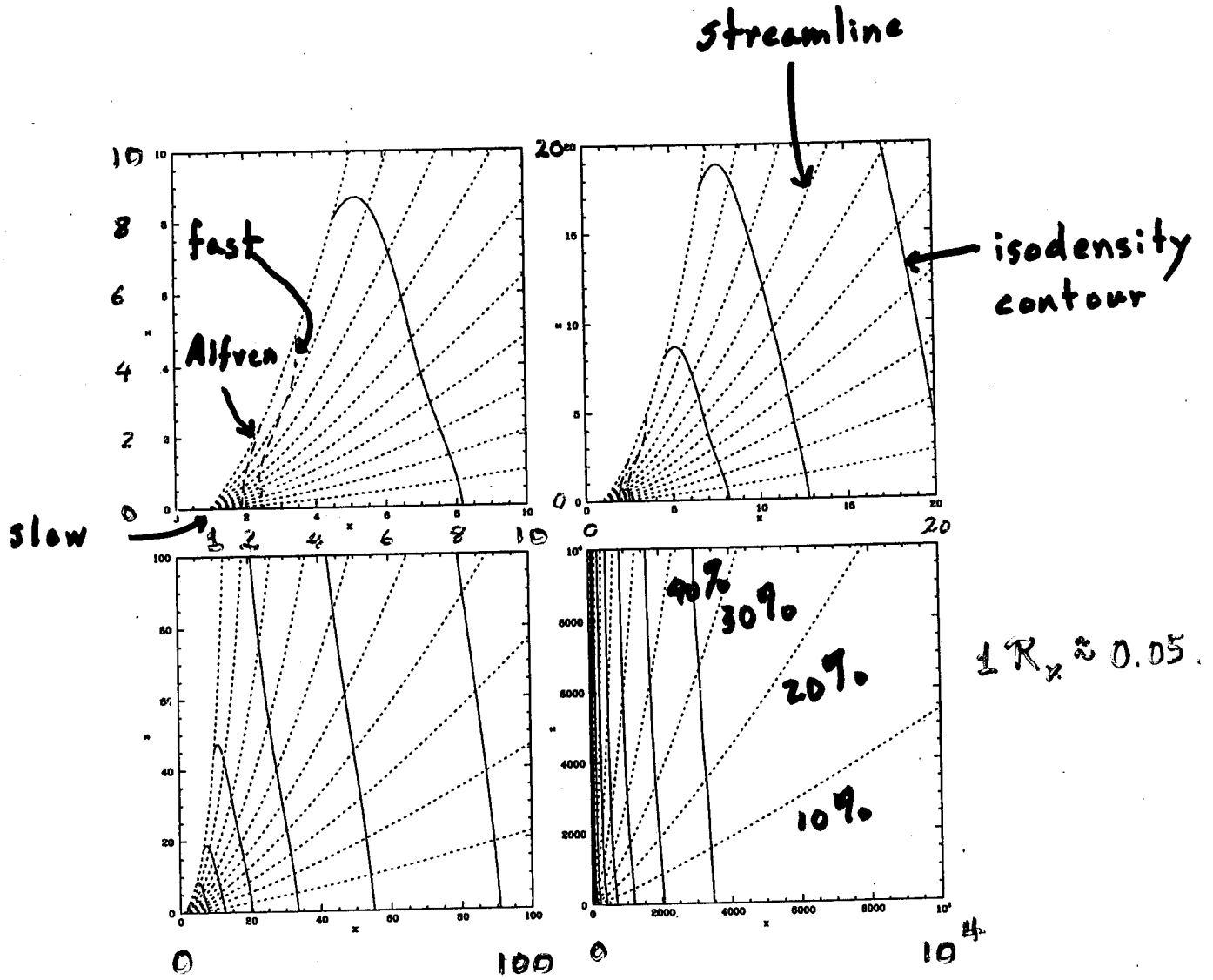
Figure 2. Isodensity contours (solid curves) and streamlines (dotted curves) for a cold x-wind with $\beta(\psi) = \beta_0(1 - \psi)^{-1/3}$, where $\beta_0 = 1$. Isodensity contours are spaced logarithmically in intervals of $\Delta \log_{10} \rho = 0.5$, and streamlines are spaced so that successive dotted lines contain an additional 10% of the total mass loss in the upper hemisphere of the flow. The loci of the Alfvén and fast surfaces are marked by dashed lines. The empty space inside the uppermost streamline, $\varpi \leq \varpi_1$, is filled with open field lines from the central star that asymptotically have the field strength, $B_z = 2\bar{\beta}/\varpi_1^2$.

Johns & Basri (1995)

Hα

Hβ
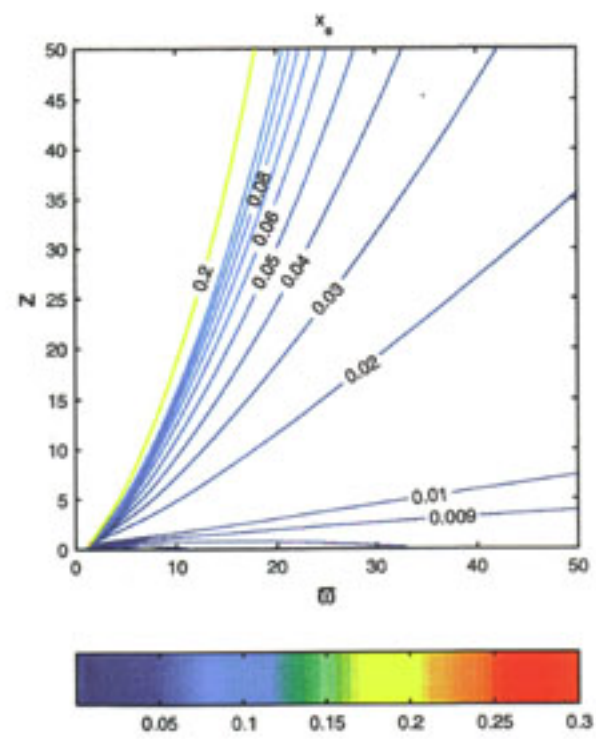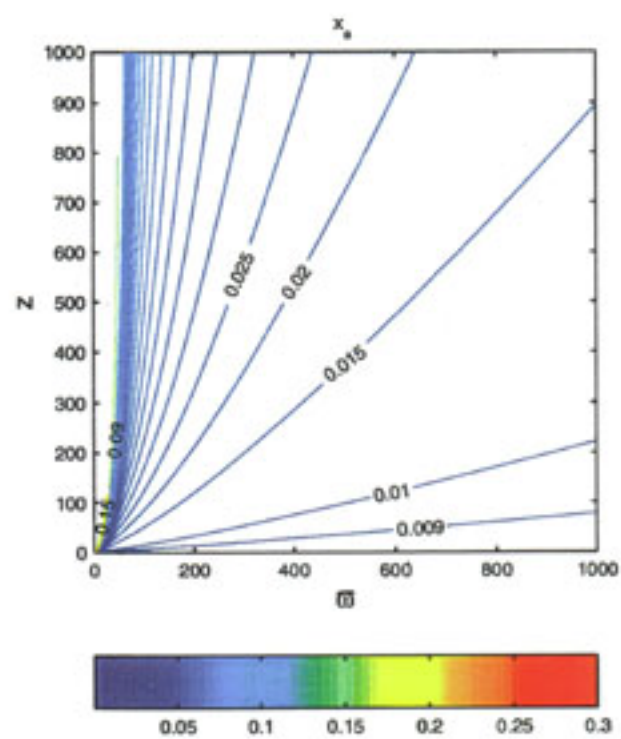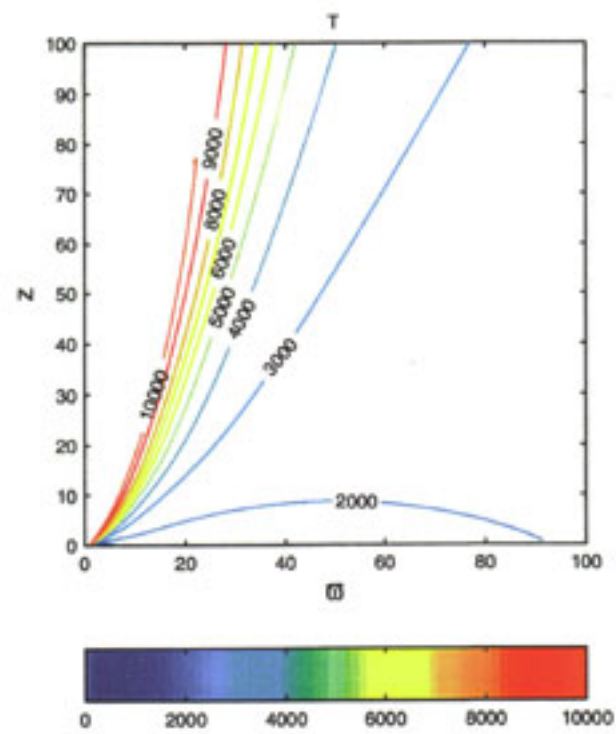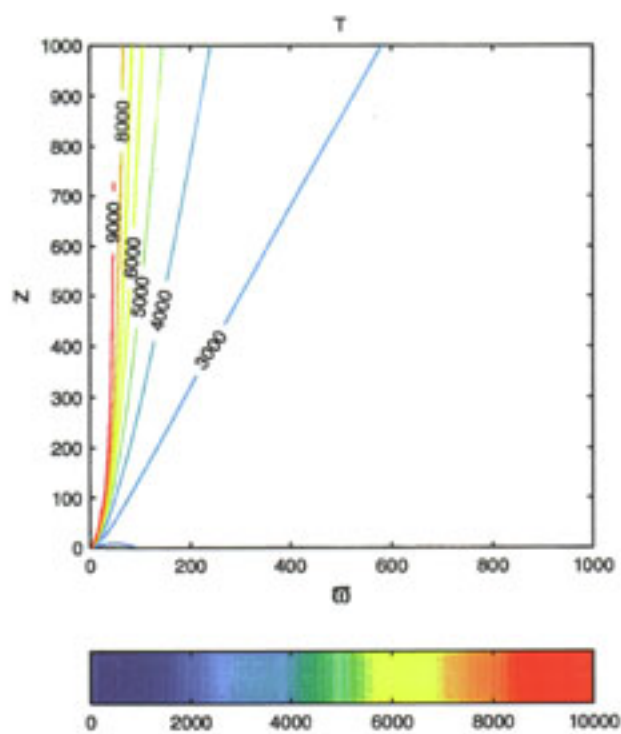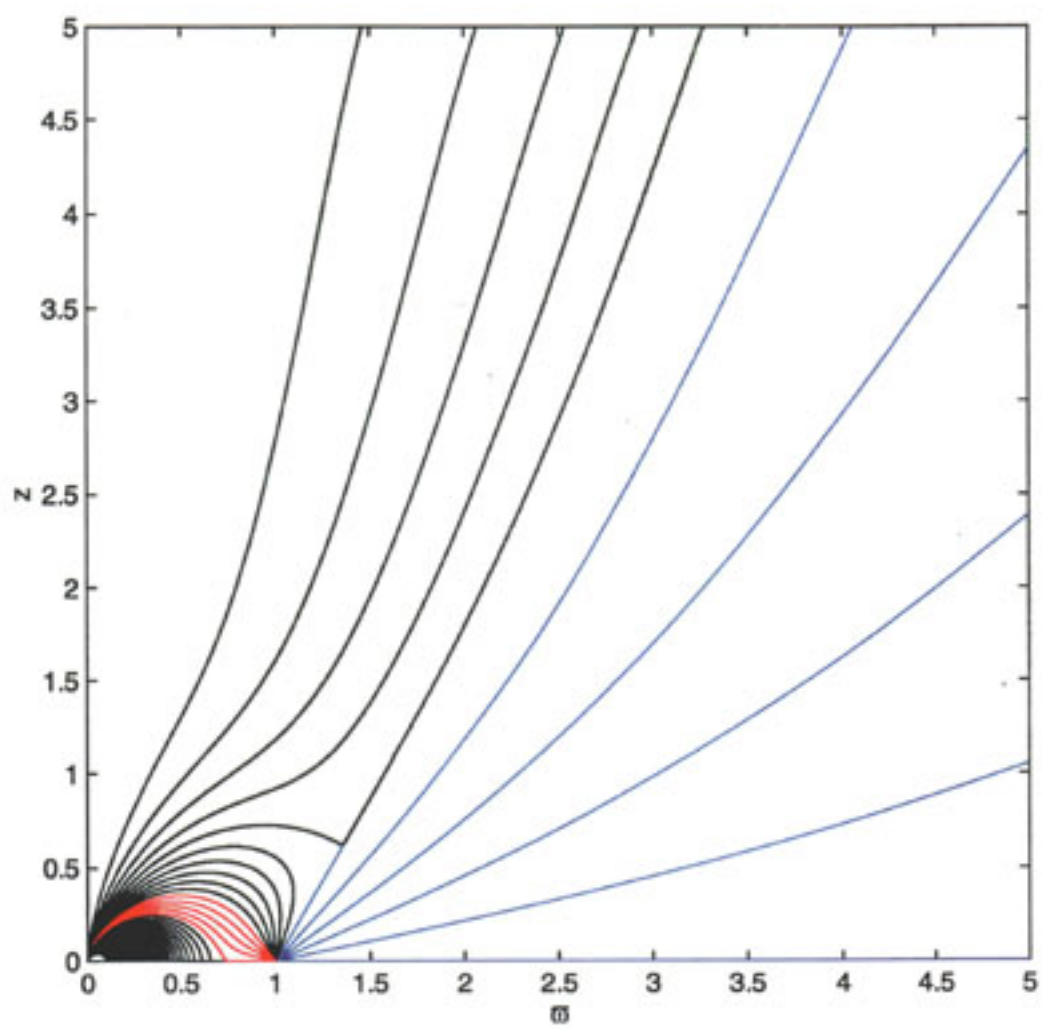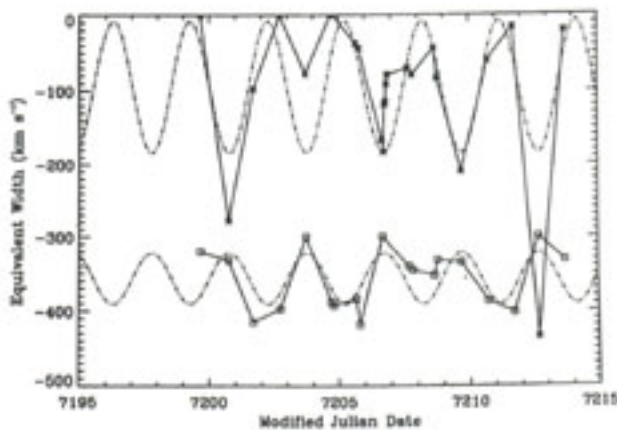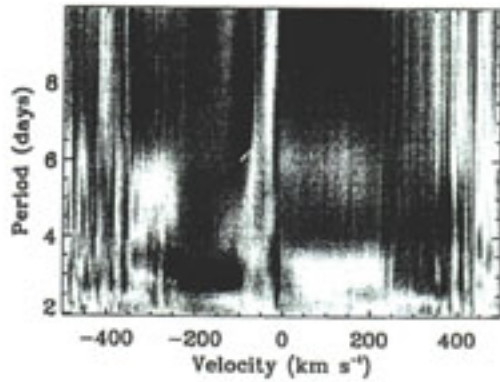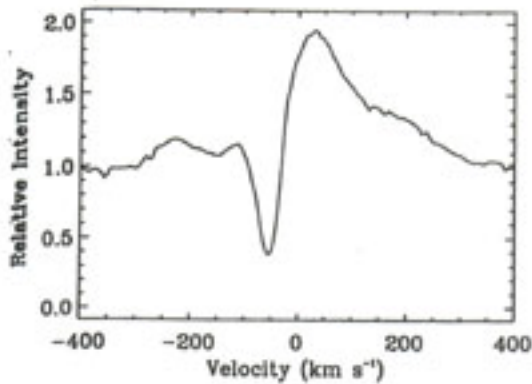
FIG. 5.—The equivalent width of the $v \sim -150$ km s^{-1} feature seen in Hα (asterisks), and the equivalent width of the $v \sim +100$ km s^{-1} feature seen in Hβ (squares), both for the 1988 February observing run. All equivalent widths are calculated from the profile fit parameters, and the Hβ equivalent widths have been offset by 300 km s^{-1} for clarity. Also shown are sine wave fits (dashed and dotted lines) to each time series, which are $\sim 180°$ out of phase.
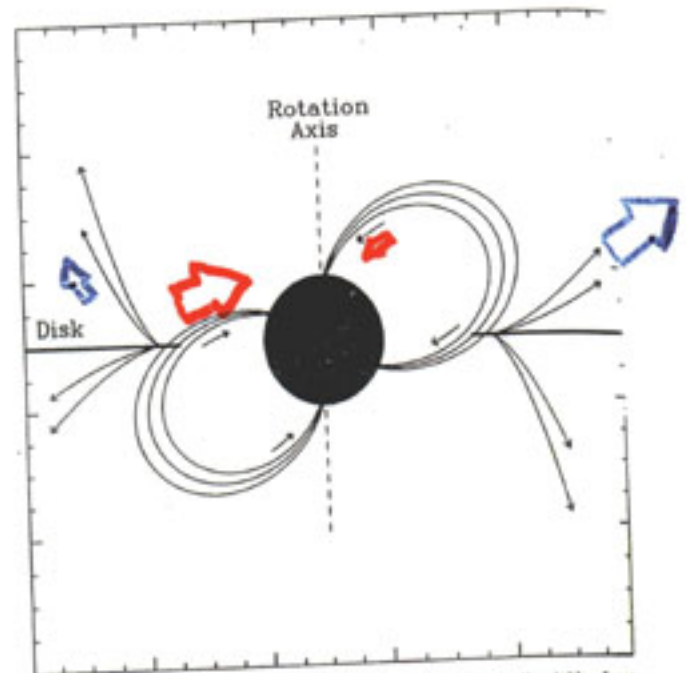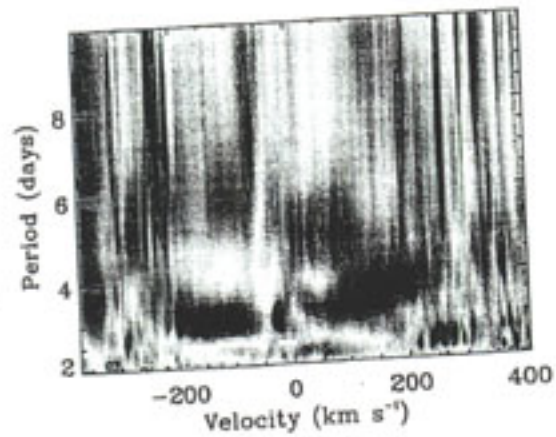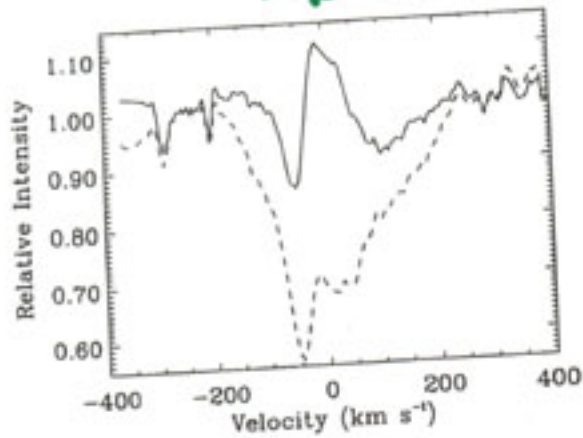
FIG. 15.—The eggbeater model adapted from the generalized X-celeration model of Shu et al. (1994). When the observer is to the right (above the disk) the wind is launched more easily than the accretion flow. A half-rotation later the accretion flow is fed more easily than the wind.

WHY EARTHS ARE PROBABLY RARE

1. Gas giants like Jupiter and Saturn probably form in nebular disks on a time scale comparable to or shorter than the few million years that nebular disks are seen to survive around typical T Tauri stars. This time scale is significantly shorter than the 10^8 yr timescale that numerical simulations indicate is needed to assemble the terrestrial planets, and the few times 10^8 yr which the lunar record shows that the primitive Moon was subject to heavy bombardment by meteoroids.

2. If gas giants form early and later migrate into the terrestrial planet-forming zone, the consequences for the orbital stability of the latter would be disastrous. If orbital migration is as common as seems to be indicated in some theoretical calculations, and as may be suggested by the finding of numerous Jupiter-like bodies well within the ice-line of their star systems, then terrestrial planets with solar-system like configurations may be quite rare. Perhaps the Earth is a happy accident that Jupiter fo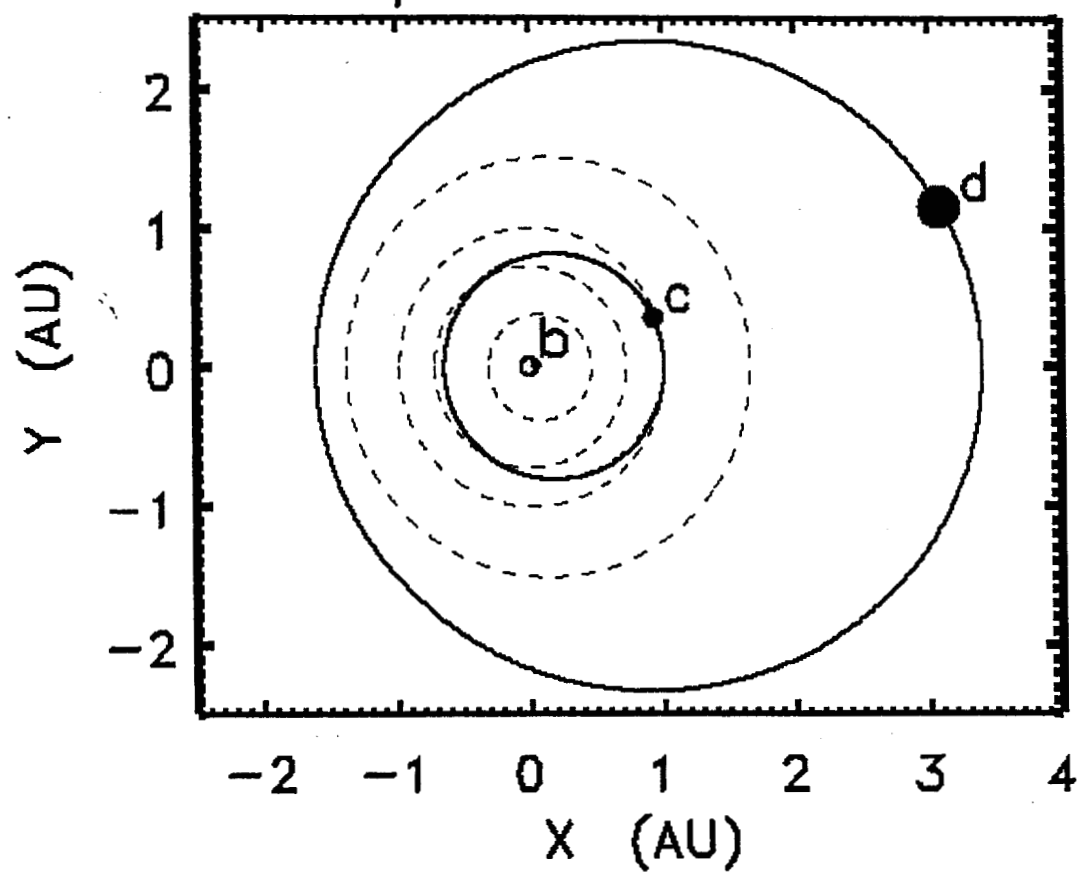rmed in our solar system only relatively late in the evolution of the solar nebula, when there was relatively little mass left in the disk to force significant orbital migration of Jupiter.

3. Even if planets with stable rocky surfaces exist around other stars, the habitable zone (where water can exist as a liquid on the planet's surface) appears to be quite narrow in the best calculations. Indeed, even for the Earth itself, it remains a puzzle why the climate was so temperate during its first couple of billion years (the faint early-sun paradox).

4. If conditions for Earthlike planets with lifeforms capable of evolving at least one species with high technological capability is as common as some SETI enthusiasts would have us believe, then "why aren't they here?" (Fermi's paradox).

5. Both thesis and antithesis that Earths are common and that Earths are rare have compelling arguments (and zealous adherents) on their sides. In such a situation, further theoretical argument is useless. We need good scientific experiments. The Terrestrial Planet Finder (TPF) Mission is NASA's response to this challenge for the beginning decades of the twenty-first century.

Upsilon Andromedae

Bryden & Lin (1998)

Coronal
Wind

Helmet Streamer

Coronal
Wind

Helmet
Dome

Soft
X-Rays

Funnel Flow

CAI Precursors

Soft
X-Rays

Dipole
Field

Star

Reconnection
Ring

X-Region

X-Wind

Chondrules

Accretion Disk
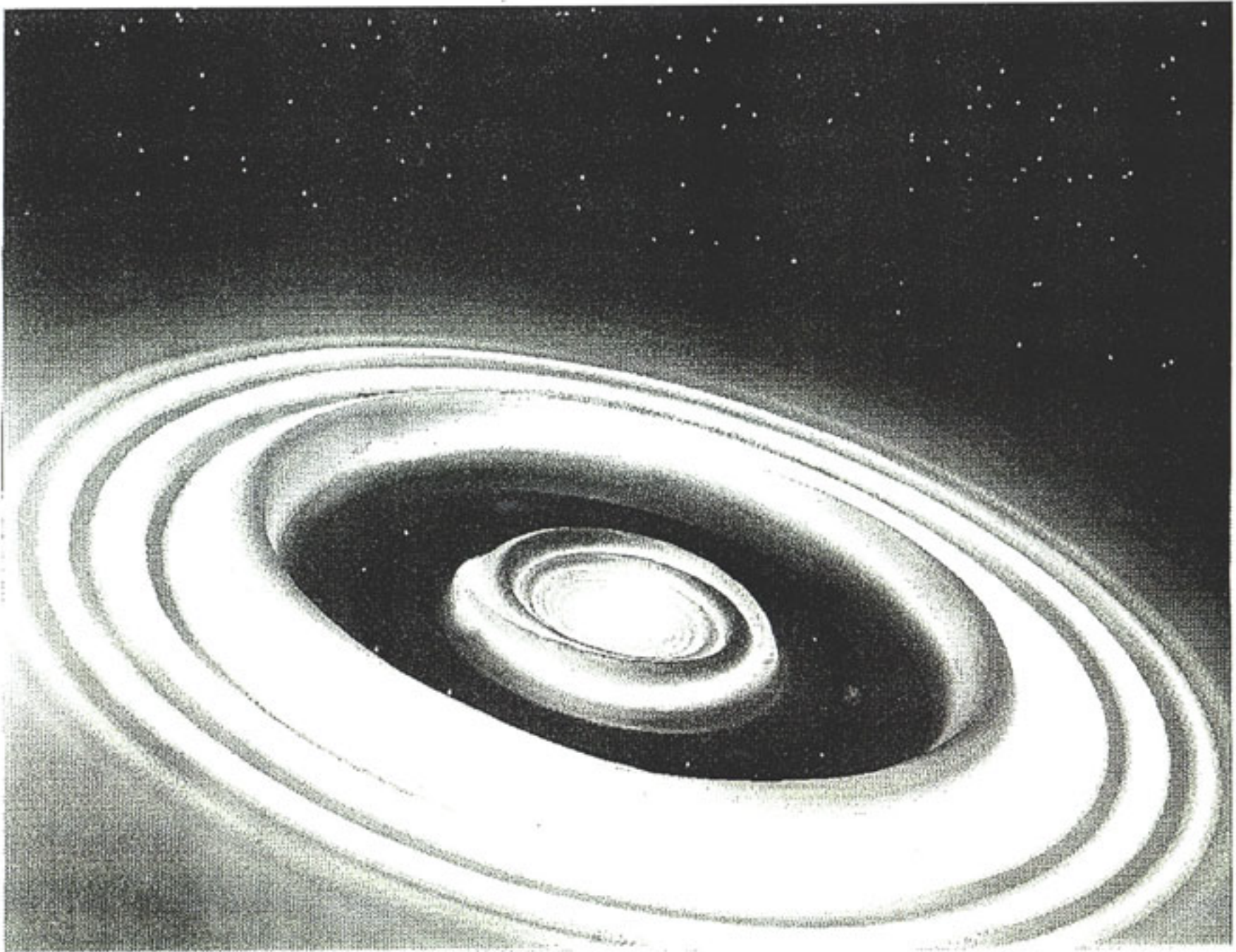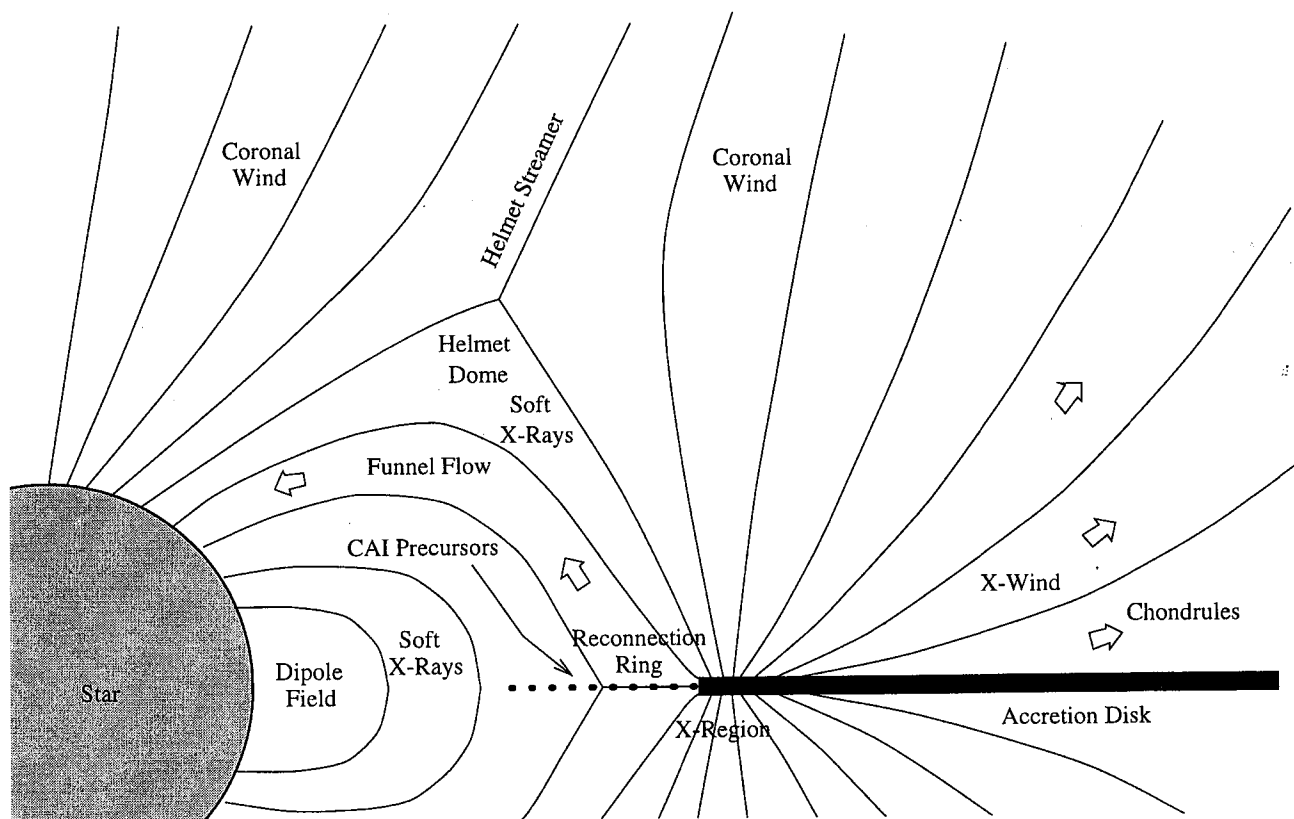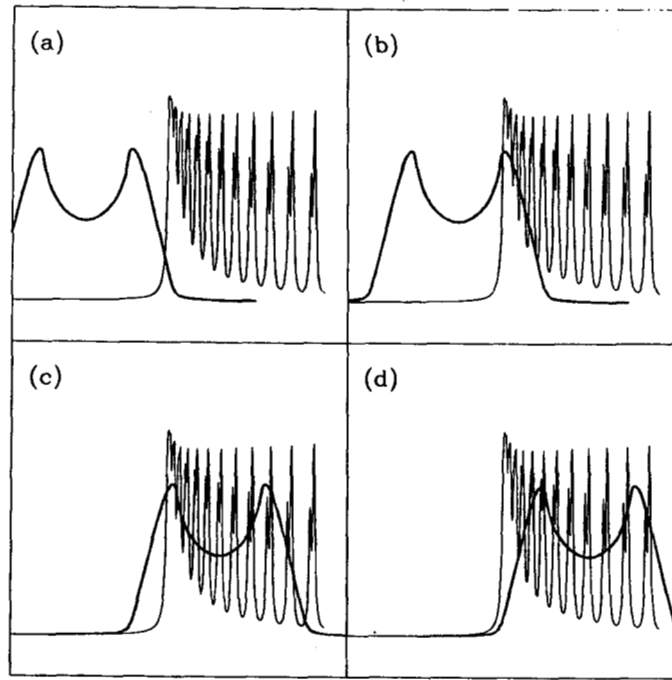
FIG. 2.—Schematic depiction of the convolution of the double-horned rotational broadening function (*heavy line*) with the rest distribution of lines near the band head (*light line*). The rotational broadening function is the profile of an isolated line from an inclined Keplerian disk that has a monotonically decreasing intensity distribution between an inner and outer radius. The rest spectrum of lines near the band head includes line blending due to local line broadening sources and assumes LTE level populations at a characteristic inner disk temperature.
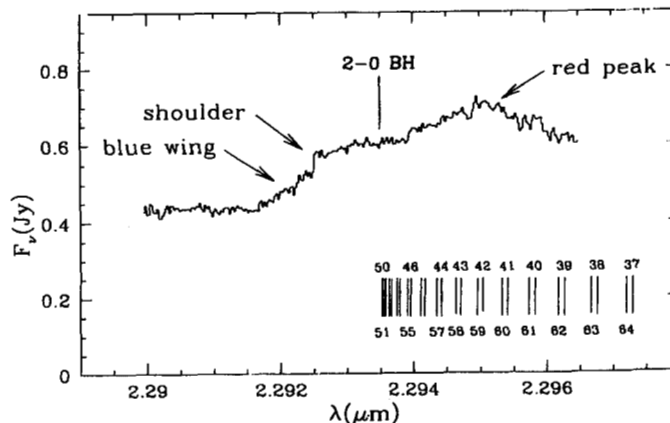
FIG. 1.—The $v = 2$–0 band head emission from WL 16 which shows the characteristic shape of band head emission from a rotating disk: a blue wing, a shoulder, and an intensity peak redward of the band head. The spectral region covered by our observations includes the R39–R62 lines.

What is $\bar{J}_*$?

Inner holes: Meyer, Calvet, & Hillenbrand (1997)

Magnetospheric Accretion: Bertout et al. (1988), Königl (19

Edwards et al. (1993, 1994), Hartmann et al. (1994) NCT MCH
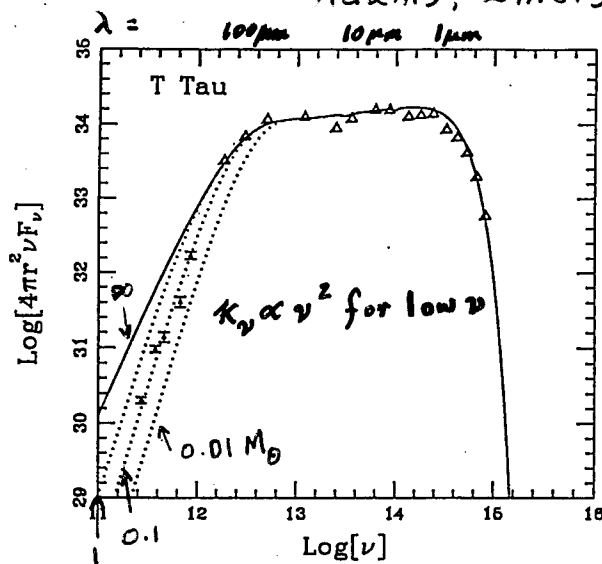
FIG. 1a
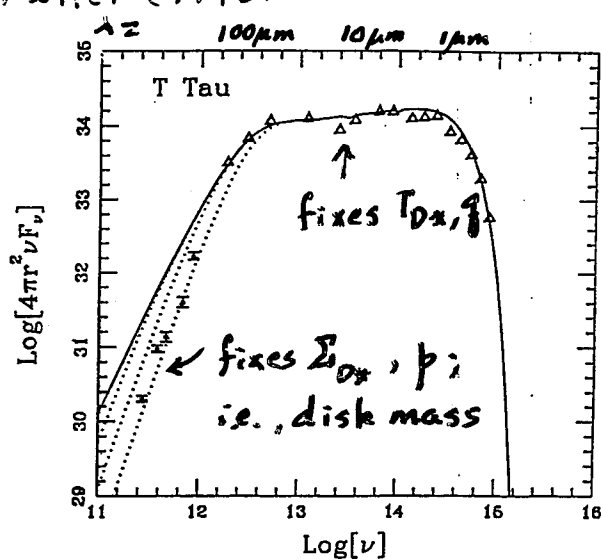
FIG. 1b
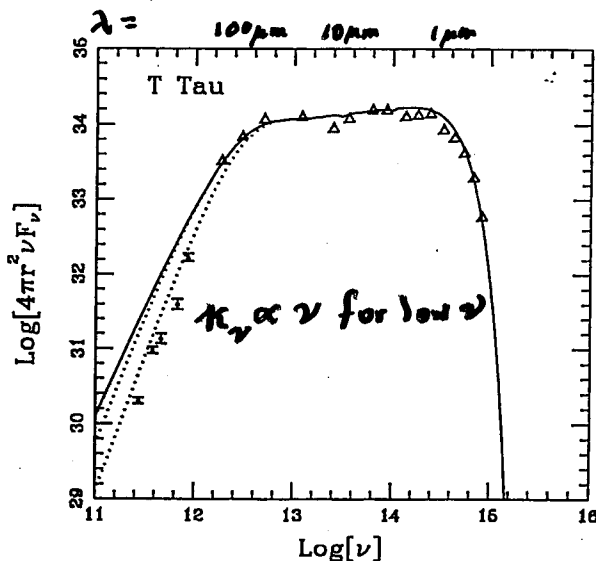
FIG. 1c

FIG. 1.—Spectral energy distribution of the infrared source T Tauri (⋅ units). Open triangles are previously observed data points, solid triangles w⋅ error bars are the data points from this paper. Where no error bars are sho⋅ they are smaller than the plotting symbols. Solid curve shows the theoreti⋅ spectrum in the optically thick ($M_D \to \infty$) limit; dotted curves show spectra f⋅ finite disk masses of 0.01, 0.1, and 1.0 $M_\odot$. (a) Models with "standard" opac⋅ law $\kappa_\nu \sim \nu^2$ at low frequencies. (b) Models with alternate opacity law $\kappa_\nu \sim \nu$ ⋅ at low frequencies. (c) Models with alternate opacity law $\kappa_\nu \sim \nu^1$ at low f⋅ quencies.

$$T(\varpi) = T_{D*} \left(\varpi / R_* \right)^{-q}$$

$$\Sigma(\varpi) = \Sigma_{D*} \left(\varpi / R_* \right)^{-p}$$

$$\text{for } R_* \leq \varpi \leq R_D = 120 AU$$

Survey by Beckwith, Sargent, Chini, + Gusten (1990):
$$T(\varpi) = T_1 \left(\varpi / 1 AU \right)^{-q} \quad \text{with } T_1 \sim 100 K \text{ and}$$
$$0.50 \leq q \leq 0.75$$

gives flat $\nu F_\nu \propto \nu^0$ at IR

classical accretion disk gives $\nu F_\nu \propto \nu^{4/3}$ at IR

Beckwith et al. found few systems with $q = 0.75$.

Possible resolution: "flat-spectrum" sources contaminated b⋅ residual infall viewed~pole-on. (Kenyor ⋅

SED of an Unobscured Thin Disk

$\hat{k}$ $\mu \equiv \cos i$
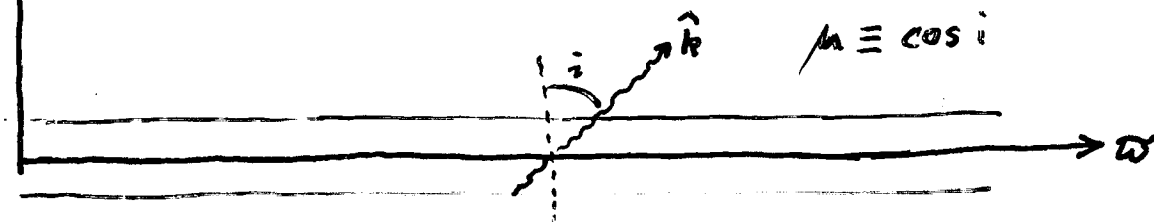
If $T = T(\varpi)$ independent of z (an approximation and disk is thin in z-direction, ray path intercep disk all of nearly same temperature (as long as $\mu \gtrsim$ In this simplified case, formal solution

$$I_\nu(\hat{k}, \tau_\nu) = I_\nu(\hat{k}, 0)e^{-\tau_\nu} + \int_0^{\tau_\varpi} B_\nu(T)e^{-\tau_\nu'}d\tau_\nu'$$

acquires the form:

$$I_\nu(\mu, \varpi) = B_\nu[T(\varpi)](1 - e^{-\tau_\nu}) \quad \text{where} \quad \tau_\nu = k_\nu \Sigma(\varpi)$$

with $\Sigma(\varpi) = \int_{-\infty}^{\infty} \rho(\varpi, z)dz$ equal to the local surfa

density of the disk. (We have assumed $k_\nu = k_\nu($

if T does not vary with z.)

$$4\pi r^2 F_\nu^D = 4\pi \int_{R_*}^{R_D} B_\nu[T(\varpi)]\{1 - \exp[-k_\nu \Sigma(\varpi)/\mu]\} \mu \varpi d\varpi$$

$\nearrow$

unattenuated flux received by observer

at distance r and direction $\mu = \cos i$

$\mu = 0.05$

Density vs. Radius

a.

log ρ , g cm⁻³ — $\log \rho$, g cm^{-3}

shock

log r , cm

Definition of Core Radius

c.

$|d \ln\rho/d \ln r|$, 10^3

ϵ_0/ρ , 10^{11} ergs g^{-1} sec^{-1}

r/R⊙

Velocity vs. Radius

b.

u , 10^2 km sec^{-1}

log r , cm

Temperature vs. Radius

d.

L

T_g (not resolved yet)

T_{rad}

log T, K

L/L⊙

log r , cm

Fig. 1.—Structure of the shock front near the end of the main accretion phase. All 300 grid points are plotted individually. (a) Density as a function of radius. Four different regions of the flow can be recognized: the centrally conde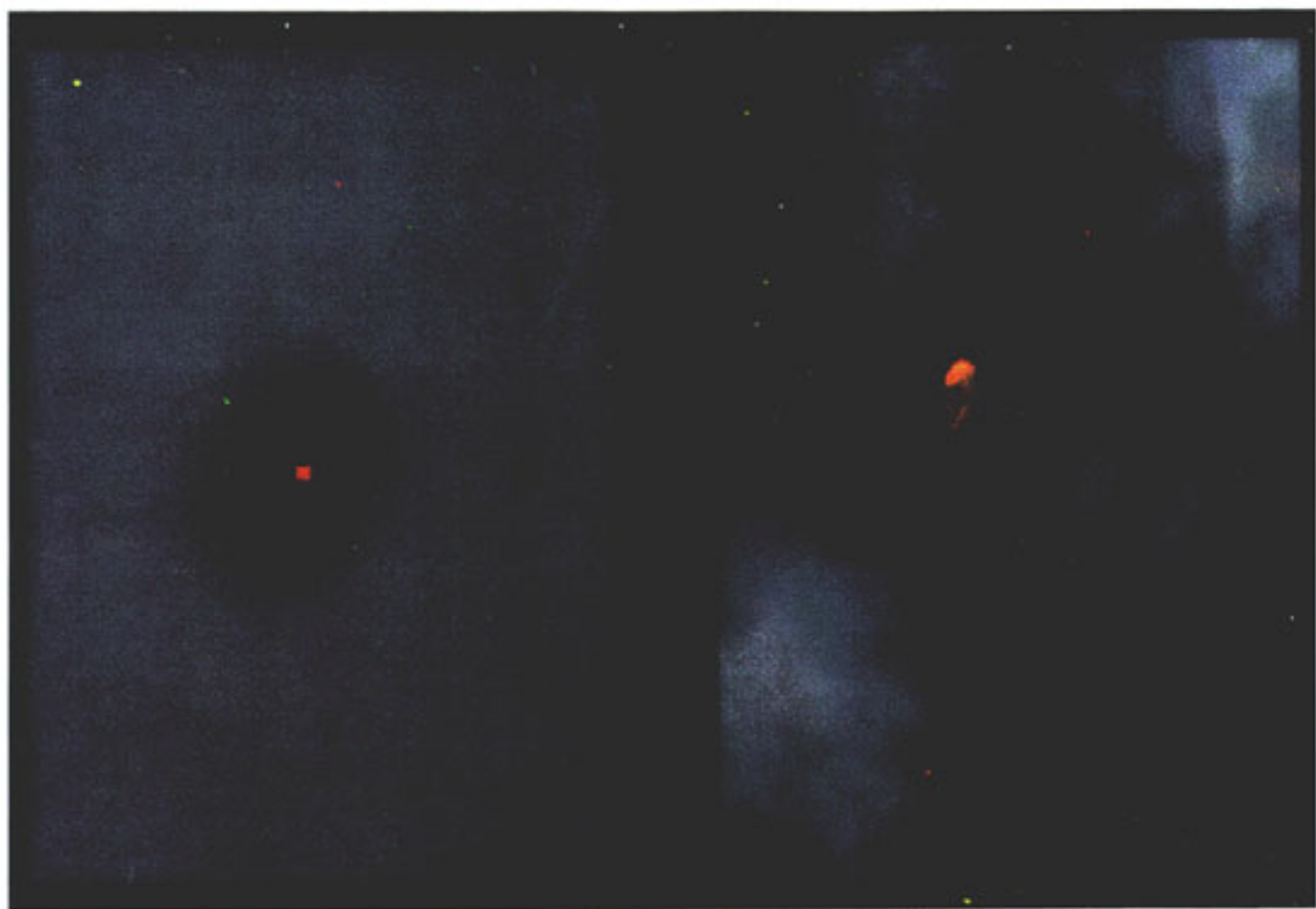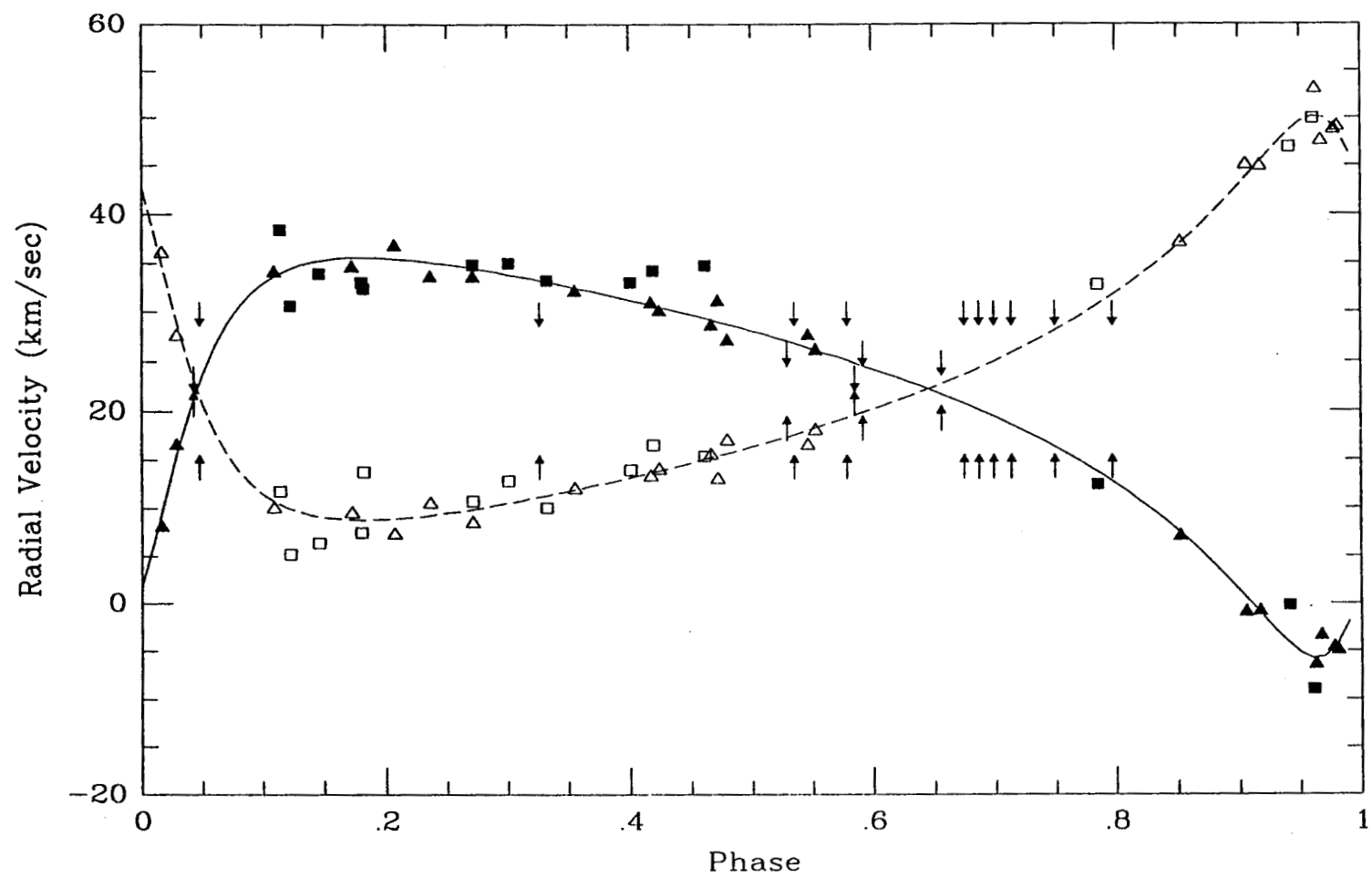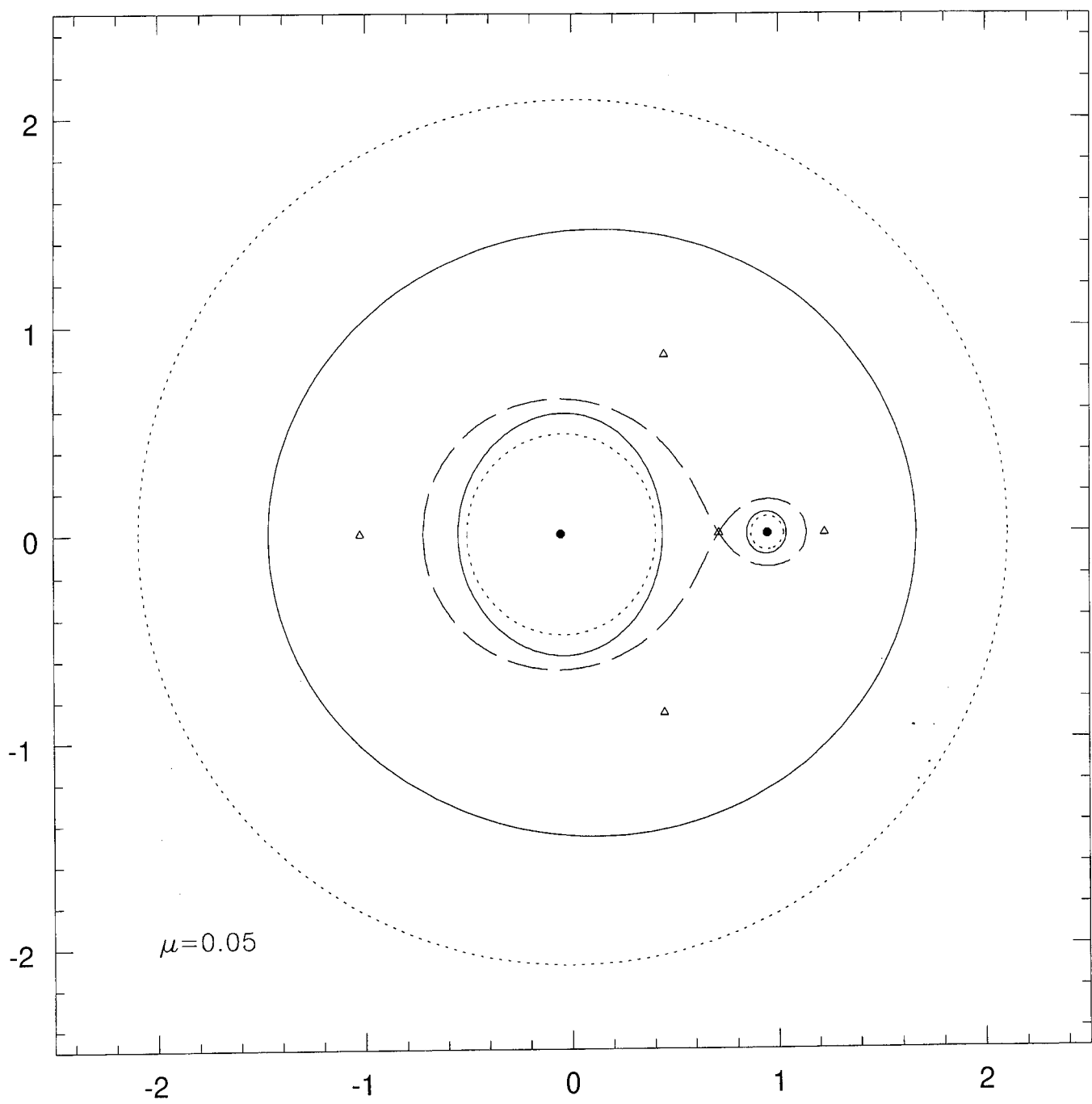nsed hydrostatic core; the exponential density decrease of the stellar atmosphere; the shock front region at $10^{-12} \le \rho \le 10^{-10}$ g cm^{-3}; and the free falling envelope in which the density falls off as $r^{-3.2}$. (b) Velocity as a function of radius. The velocity u accelerates as $-r^{-1.2}$ in the envelope; the sharp deceleration occurs in the region of the accretion shock. The stellar atmosphere in this diagram appears as a small region near zero velocity at the boundary of the hydrostatic core. (c) Definition of the core radius. The maximum in the slope $\alpha = |d \ln \rho/d \ln r|$ (triangles, left scale) of the atmospheric density drop provides a very sharply defined edge $R = R_{core}$ for the stellar core, and the maximum in the viscous energy generation rate ϵ_0/ρ (crosses, right scale) provides a satisfactory definition of the center $R = R_{shock}$ of the artificially smeared-out shock front. The luminosity L (solid line, arbitrary scale) is produced primarily in the inner portion of the shock, corresponding to the relaxation region of the temperature overshoot. (d) Temperature as a function of radius. The gas temperatures (crosses) and radiation temperature (squares) structure is shown (left scale) in the vicinity of the accretion shock. Matter and radiation are in thermal equilibrium in the core, in the atmosphere, and in the envelope. However, they decouple in the accretion shock as well as in the optically thin, essentially adiabatic preheating compression zone in front of the shock front. The luminosity (solid curve, right scale) produced in the preheating zone is negligible compared to that produced in the temperature overshoot relaxation zone, as is the contribution of the protostellar core.

Winkler and Newman

(1980)

Impossible H-R diagram track

log κ_R opacity gap

dust opacity

gas opacity

H-R Diagram

2.5×10^5 2.35×10^5 10^5 5×10^4 10^4 1

4.2×10^5

ZAMS

forbidden to any photosphere, gas or dust

optical objects

infrared objects

10^{-3}

2×10^{-7}

0

log L/L⊙

log T, K

Density vs. Radius (a.)

shock

Definition of Core Radius (c.)

Velocity vs. Radius (b.)

Temperature vs. Radius (d.)
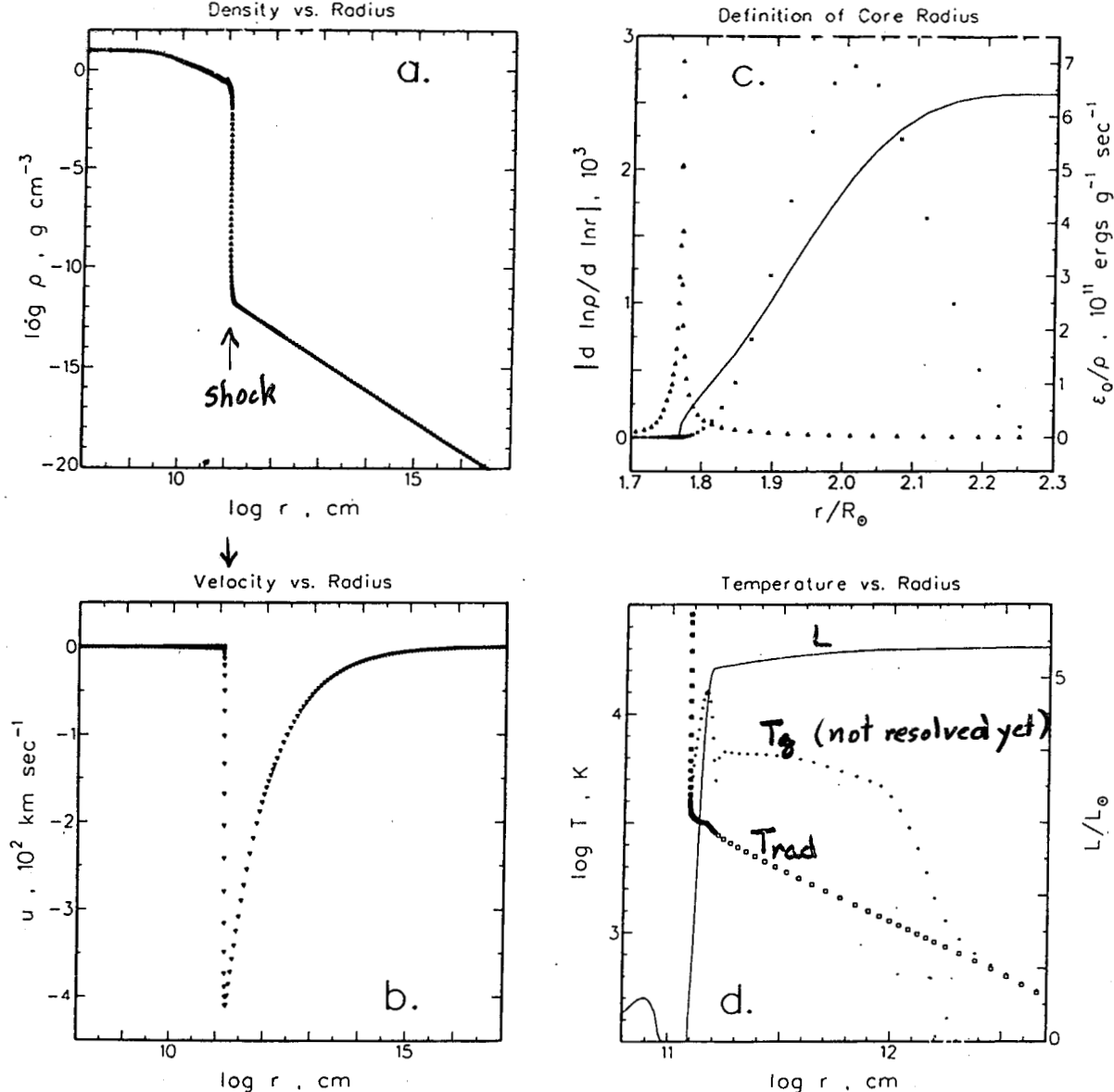
L

T_g (not resolved yet)

T_{rad}

Fig. 1.—Structure of the shock front near the end of the main accretion phase. All 300 grid points are plotted individually. (*a*) Density as a function of radius. Four different regions of the flow can be recognized: the centrally condensed hydrostatic core; the exponential density decrease of the stellar atmosphere; the shock front region at $10^{-12} \leq \rho \leq 10^{-10}$ g cm^{-4}; and the free falling envelope in which the density falls off as $r^{-3\cdot2}$. (*b*) Velocity as a function of radius. The velocity u accelerates as $-r^{-1\cdot2}$ in the envelope; the sharp deceleration occurs in the region of the accretion shock. The stellar atmosphere in this diagram appears as a small region near zero velocity at the boundary of the hydrostatic core. (*c*) Definition of the core radius. The maximum in the slope $\alpha = |d \ln \rho / d \ln r|$ (*triangles*, left scale) of the atmospheric density drop provides a very sharply defined edge $R = R_{core}$ for the stellar core, and the maximum in the viscous energy generation rate ϵ_0/ρ (*crosses*, right scale) provides a satisfactory definition of the center $R = R_{shock}$ of the artificially smeared-out shock front. The luminosity L (*solid line*, arbitrary scale) is produced primarily in the inner portion of the shock, corresponding to the relaxation region of the temperature overshoot. (*d*) Temperature as a function of radius. The gas temperatures (*crosses*) and radiation temperature (*squares*) structure is shown (left scale) in the vicinity of the accretion shock. Matter and radiation are in thermal equilibrium in the core, in the atmosphere, and in the envelope. However, they decouple in the accretion shock as well as in the optically thin, essentially adiabatic preheating compression zone in front of the shock front. The luminosity (*solid curve*, right scale) produced in the preheating zone is negligible compared to that produced in the temperature overshoot relaxation zone, as is the contribution of the protostellar core.
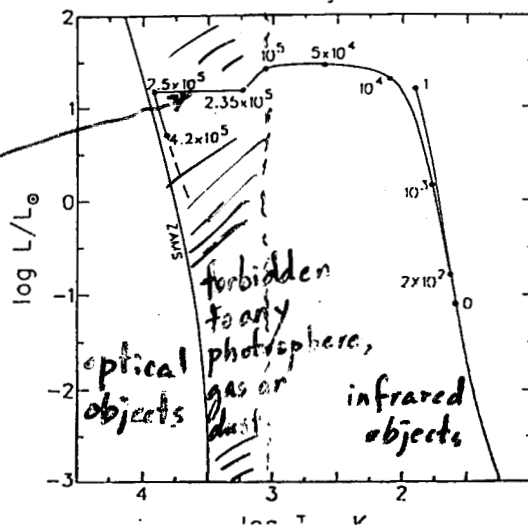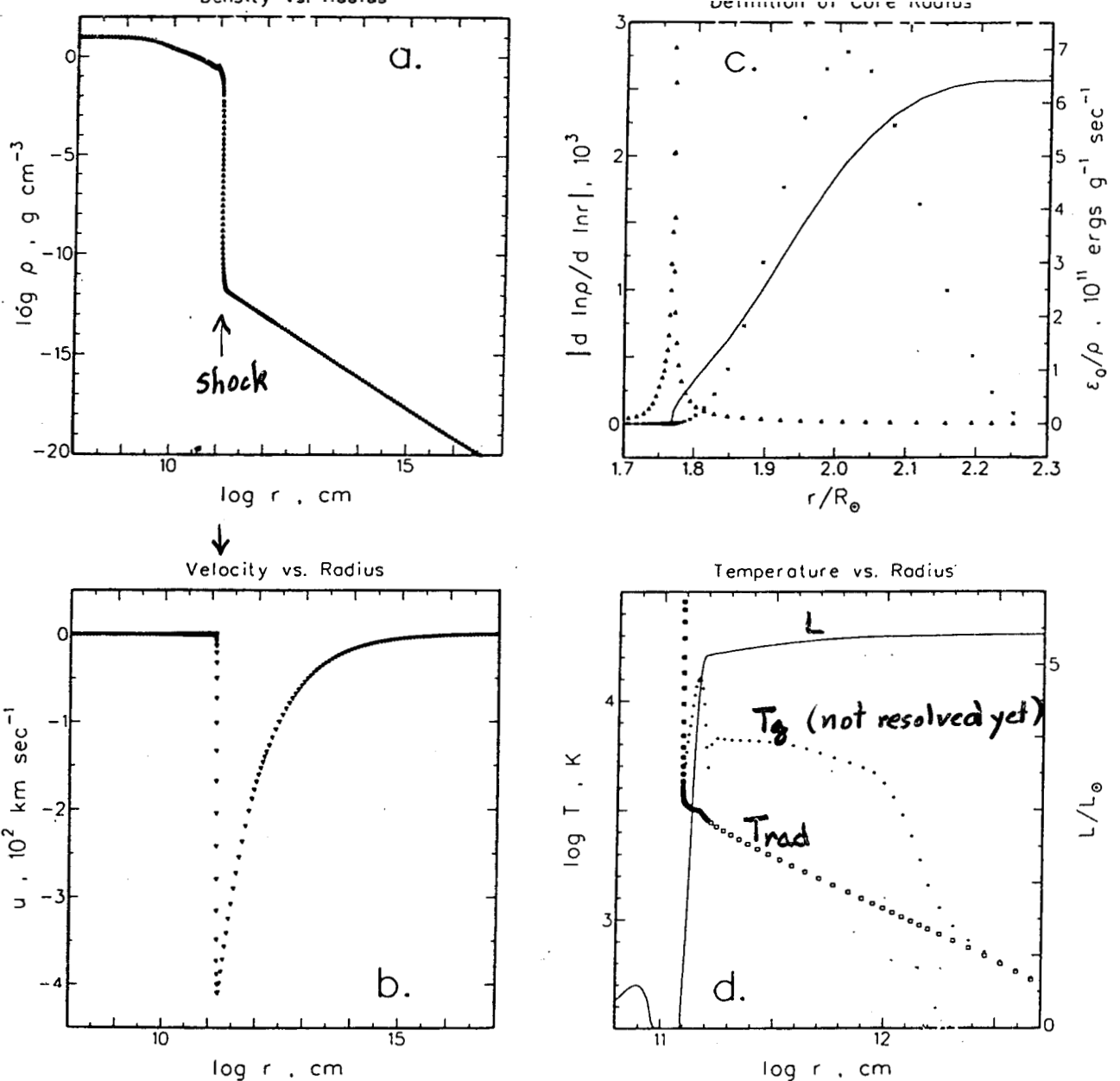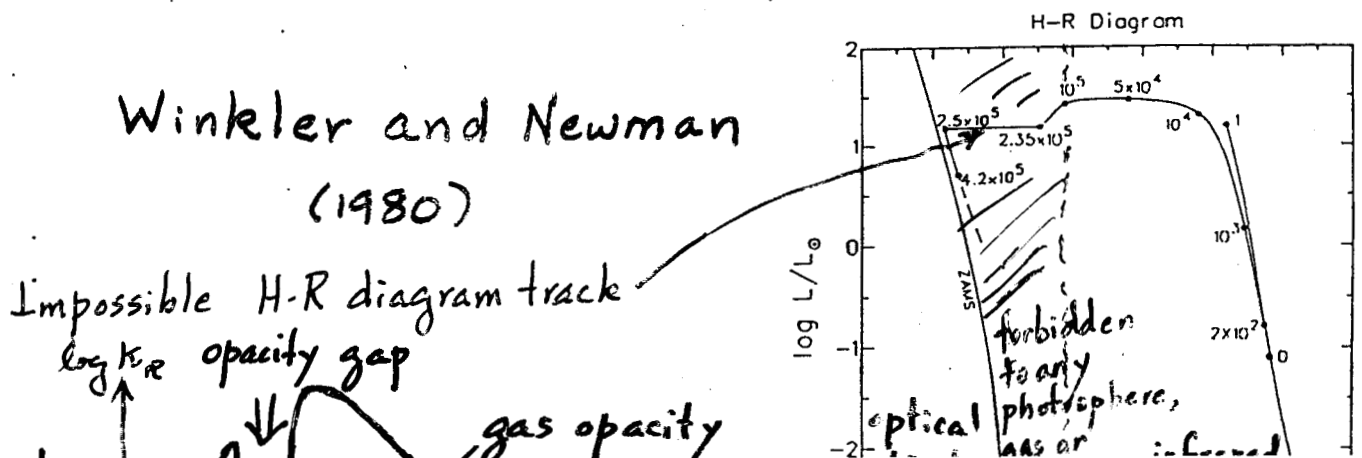
Winkler and Newman
(1980)

Impossible H-R diagram track

$\log \kappa_R$ opacity gap

gas opacity

H-R Diagram

2.5×10^5 2.35×10^5
4.2×10^5
10^5 5×10^4
10^4 1
10^{-1}
2×10^2 0

ZAMS

forbidden to any photosphere, gas or

optical photosphere
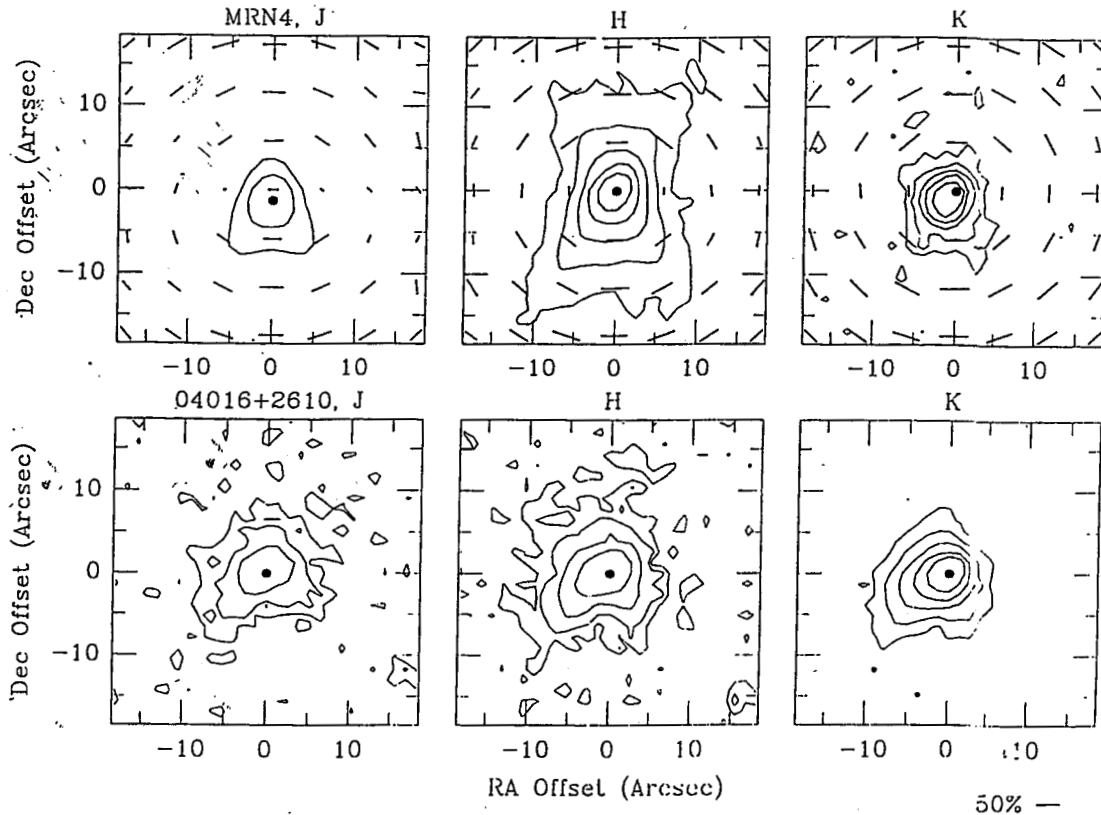
Scattered Near- IR Light

FIG. 13.—Comparison of model and observed images for the embedded *IRAS* source 04016+2610. *Upper panels*: *JHK* images for a model with $\dot{M} = 4.5 \times 10^{-6}$ $M_\odot$ yr^{-1}, $R_c = 40$ AU, $\theta_H = 31°$, and $i = 60°$. *Bottom panels*: *JHK* observations of 04016+2610.

SED of

IRAS 04016+2610

$\dot{M} = 4 \times 10^{-6}\, M_\odot yr^{-1}$
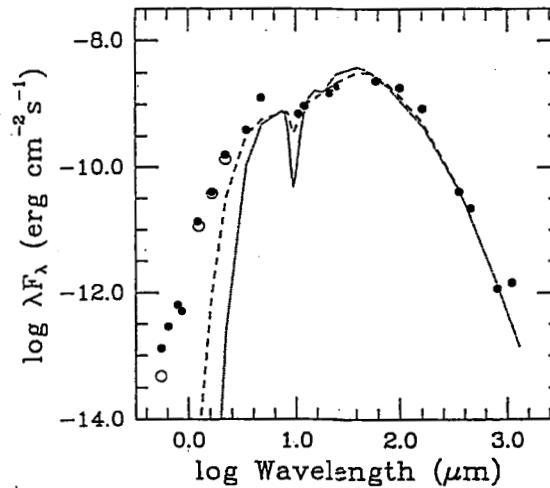

FIG. 14.—Comparison of observed and model spectral energy distributions for the embedded *IRAS* source 04016+2610. The filled circles represent the observed data, while the dashed and dotted lines plot one-dimensional models from Paper I. The open circles indicate predicted fluxes for the scattering models.

Kenyon, Calvet, & Hartmann (1993)

Kenyon, Whitney, et al. (1993)

two colliding winds has recently been given by Wilkin (1996) and Canto, Raga, & Wilkin (1996). All one needs to specify is the mass loss rates and speeds of the two winds, and the separation of the two wind sources.

The extent to which the planetary wind will be blown back by the stellar wind is given as a function of the parameter β, which is $\frac{M_P v_P}{M_S v_S}$. Our best estimate of the value of β is therefore 5×10^{-3}. This leads to an opening angle of the planetary hydrogen tail of about $20°$ (Fig. 1). Because this angle only depends on the cube root of β, it is not likely to be far wrong. The angle is not likely to be less than $12°$ or more than $30°$. In the simple theory, the wind will continue to open with that angle indefinitely, which would guarantee an eclipse so long as the orbital inclination to the line of sight was less than this opening angle. In practice, the line of sight will intersect the wind within a star-planet separation D or two if it is going to intersect at all (except in a very small range of grazing angles). Thus our angle estimate is a convincing limit on the range of orbital inclinations allowed. These angles are 2-5 times larger than the angles allowed by direct eclipses of the planets themselves. *[handwritten: Fig. 1]*
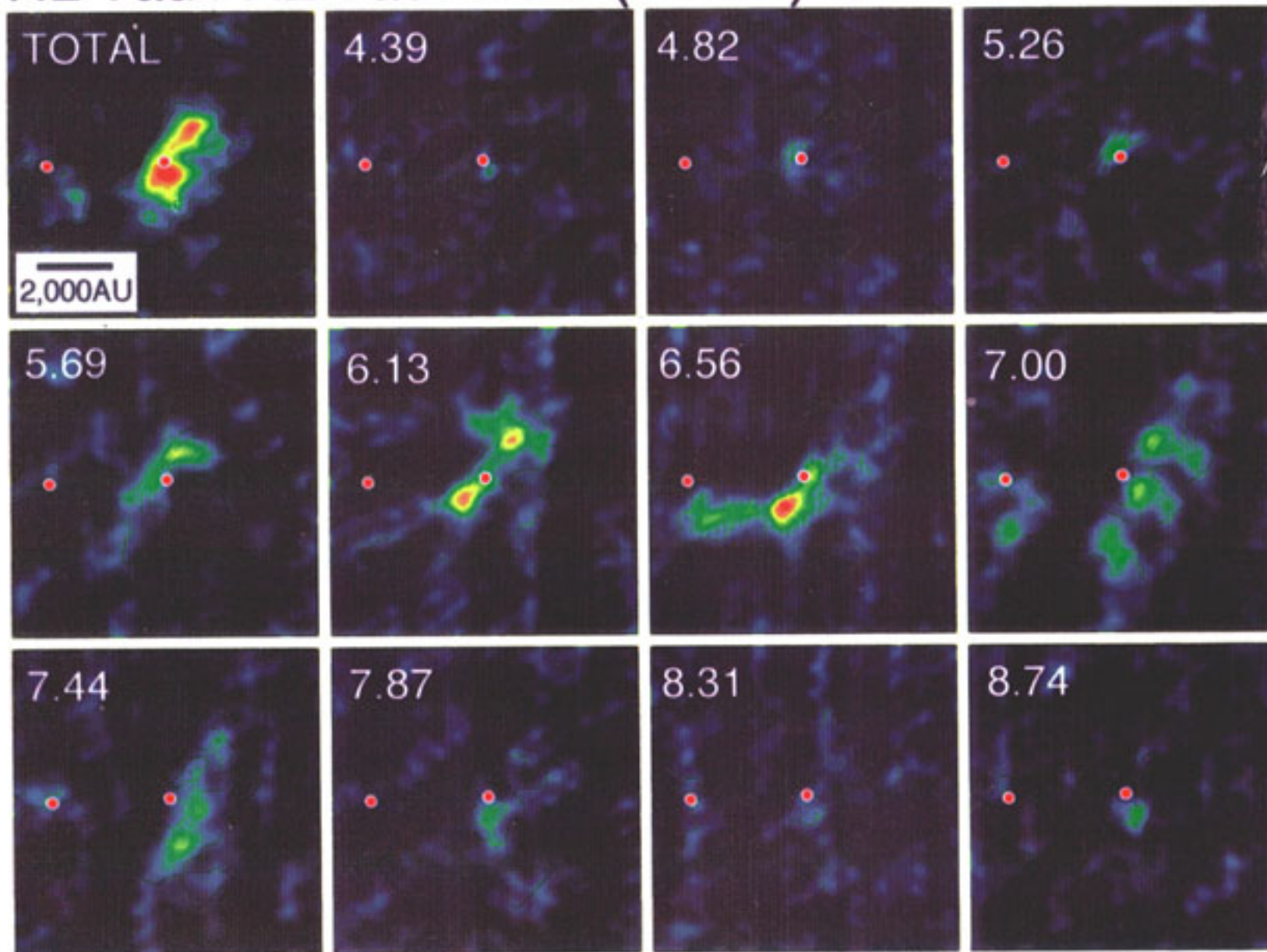
Of course, there is likely to be a planetary magnetosphere, and the stellar wind also contains a magnetic field, which introduces uncertainty in the estimation. If the planet is like Jupiter, we can expect a substantial magnetic field. One can argue it will be somewhat weaker than Jupiter's because these planets are tidally locked to their stars and so will have rotation periods a factor of 10 slower than Jupiter. In stars (and planets), the magnetic flux produced by the dynamo is proportional to the rotation rate. Furthermore, the convective motions internal to the planets are likely to be less vigorous than in Jupiter because of their strong surface heating. Jupiter's "magnetodisk" extends to 50 R_J or more, and a weaker field strength combined with the far higher rate of exospheric particle emission would serve to inflate the magnetosphere still further. The magnetic fields help couple the winds, so we expect a shock between them not unlike that in the fluid theory. For neutrals the mean-free-path is about D, but for ions the gyroradius is only about 1 km.

On the other hand there is increased pressure from the stellar wind for these planets compared with Jupiter. The stellar winds might be weaker than the solar wind, since 51 Peg is less active and the other two stars are earlier spectral types with thinner convection zones. *[handwritten: (this is why they are more rapid rotators)]* The stellar wind not only affects the opening angle, but eventually acts to force the tail to stop opening and flow radially outward. Because of the high mass flux from the extrasolar planets, their tails are relatively "stiff", and we find this will not occur for roughly 2-5 times the distance of the planet to the star. The planetary magnetic field also acts on the sunward side to stiffen the obstacle presented over what is assumed in the simple theory, and so will open the tail cone and allow eclipses at greater orbital inclinations. Because of the already high pressure, however, this may not help much down the tail.

The planetary hydrogen might be seen as a large absorption feature against the stellar Ly-α emission line. Essentially all the material emitted by the planet ends up in the magnetotail. We integrate Wilkin's model through the preshock gas and the denser shocked shell, obtaining a column density $\sigma_0 = 2 \times 10^{13}(\frac{N_H}{10^{34}})/[(\frac{D}{10R_\odot})(\frac{v_P}{50km/s})]cm^{-2}$. Integrating through the cloud structure then yields total columns of around 10^{15}. One needs a column several tenths of an AU long before there is as much hydrogen in it as in the rest of the ISM to the

4

HL Tau / XZ Tau ^{13}CO (J=1−0)

Hayashi, Ohashi, & Miyama (1993)

MAGNETIZED SINGULAR ISOTHERMAL DISKS (SIDs)

AND

THEIR BIFURCATIONS

Dimensionless Mass-to-Flux Ratio:

$$\lambda = \frac{2\pi G^{1/2}\Sigma}{B_z} = \text{const} \geq 1.$$

Dilution Factor for Self-Gravity Due to Magnetic Tension:

$$\epsilon = 1 - \frac{1}{\lambda^2}.$$

Enhancement Factor for Gas Pressure Due to Magnetic Pressure:

$$\Theta = \frac{\lambda^2 + 3}{\lambda^2 + 1}.$$

Notice that $\Theta \leq 2$. For unmagnetized SIDs: $\epsilon = 1$ and $\Theta = 1$.

Axisymmetric Singular Isothermal Disk

Surface Density:

$$\Sigma_0(\varpi) = \frac{\Theta a^2}{2\pi G \epsilon G \varpi}\left(1 + D^2\right).$$

Flat Rotation Curve:

$$\varpi\Omega(\varpi) = \Theta^{1/2}D.$$

Toomre Q:

$$Q = 2\sqrt{2}\frac{D}{(1+D^2)}.$$

Notice $Q = 1$ for $D = \sqrt{2} \pm 1$, and $Q = Q_{\max} = \sqrt{2}$ at $D = 1$.

Bifurcations:

$$\Sigma_1(\varpi, \varphi) = \frac{\hat{S}}{\varpi}\cos(m\varphi)$$

have solutions with $\hat{S} \neq 0$ at any D for $|m| = 1$, and at

$$D^2 = \frac{|m|}{|m| + 2} \qquad \text{for} \qquad |m| \geq 2.$$

Analogous to bifurcations of Maclaurin spheroids.

PRINCIPAL RESULTS FOR

MAGNETIZED, SINGULAR, ISOTHERMAL TOROIDS

- Density Distribution at $t = 0$:

$$\rho(r,\theta,0) = \frac{a^2}{2\pi G r^2} R(\theta),$$

with

$$\int_0^{\pi/2} R(\theta) \sin\theta \, d\theta = 1 + H_0.$$

- Magnetic Flux Distribution at $t = 0$:

$$\Phi(r,\theta,0) = \frac{4\pi a^2 r}{G^{1/2}} \phi(\theta).$$

- Mass Infall Rate for $t > 0$:

$$\dot{M} = \mathcal{M}_0 (1 + H_0) \frac{a^3}{G},$$

where $\mathcal{M}_0 = 0.975(1 + H_0)$ for $H_0 \ll 1$ and $\mathcal{M}_0 = 1.05$ for $H_0 \gg 1$.

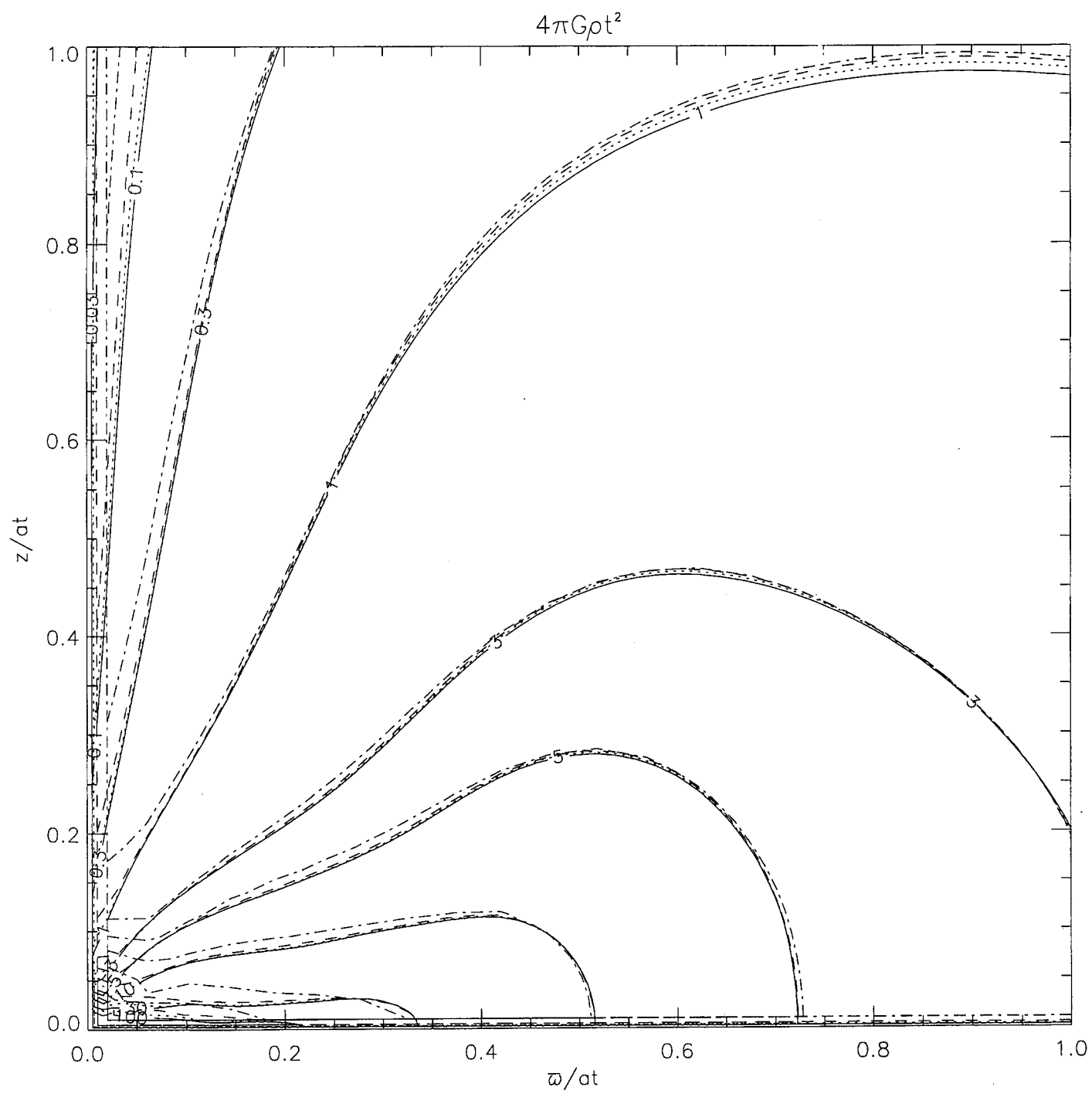- Formation of Pseudodisk for $t > 0$:

$$R_B = x_B a t,$$

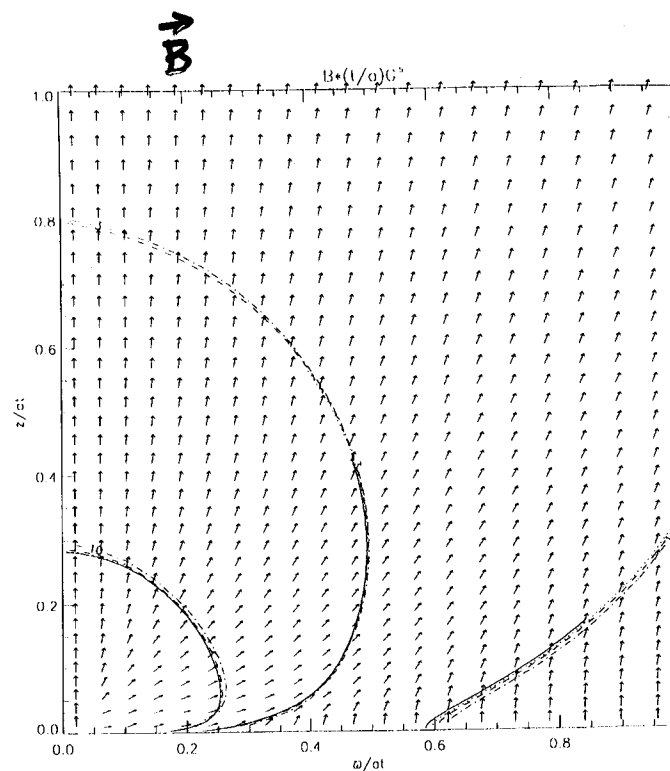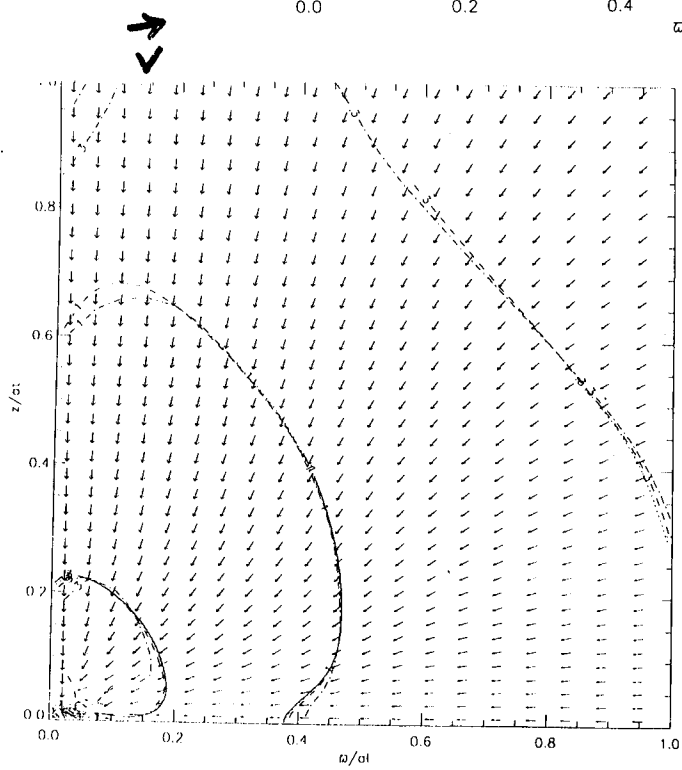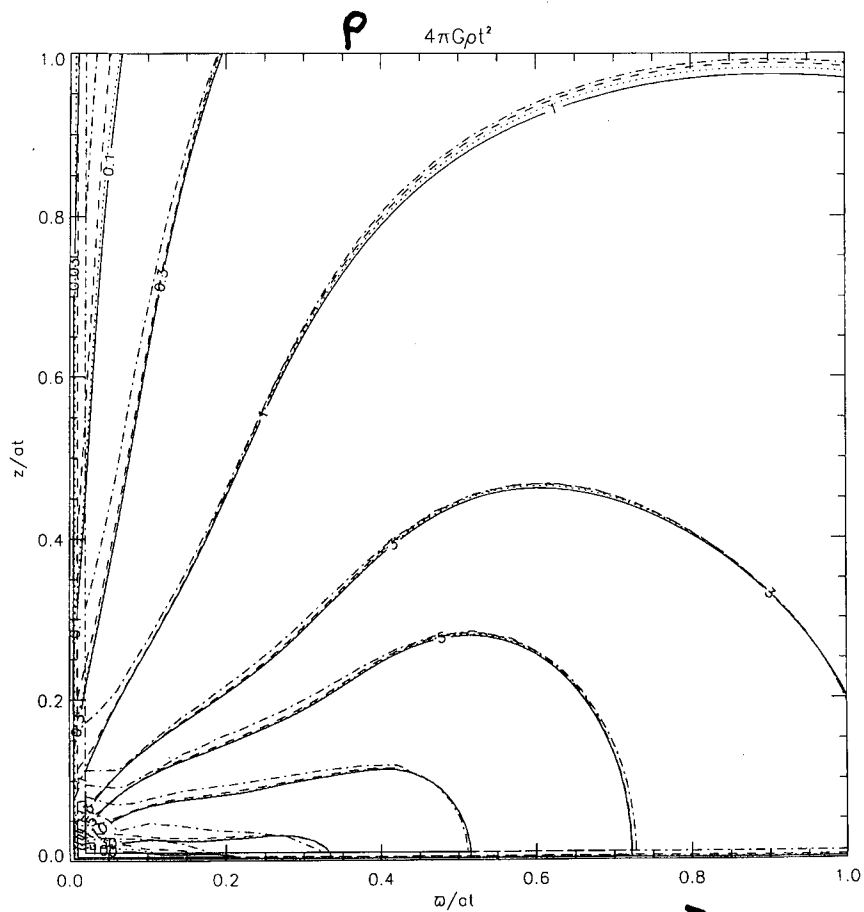with $x_B \approx 0.3$ for $H_0 = 0.25$.

- Formation of Centrifugal Disk for $t > 0$:

$$R_C = x_C a t,$$

$x_C \approx \mathcal{M}_0 \beta^2 / 4$ where rotational velocity at $t = 0$ is given by βa with $\beta \ll 1$.

Allen + Shu (2001)

BINARY STAR FORMATION – HISTORY OF IDEAS

• Newton (1686, Book III, Prop. XIX) estimates flattening of Earth due to its rotation by a perturbational analysis.

On basis of astronomical measurements, Cassini asserts Earth to be prolate rather than oblate. Maupertuis settles controversy by expedition to Lapland. Comments by Voltaire. Maclaurin (1740) gives general formula for flattening of rotating, oblate, axisymmetric, liquid spheroids.

THE FISSION HYPOTHESIS

• The slow contraction of a **uniformly rotating homogeneous spheroid** causes it to spin up faster, until the rate reaches a critical value at which a sequence of **Jacobi ellipsoids** bifurcates from the **Maclaurin spheroid** sequence (Jacobi 1834). Upon further contraction and spin-up, the Jacobi ellipsoid becomes pear-shaped (Liapunov 1884, Poincaré 1885) and fissions into two bodies (Jeans 1928 conjecture).

Two Difficulties:

1) Gaseous configurations with realistic degrees of central concentration (e.g., polytropes), which are uniformly rotating, reach equatorial break-up before Jacobi bifurcation (James 1964).

2) Differentially rotating polytropes can become bar-unstable before reaching equatorial break-up (Ostriker and Mark 1968, Bodenheimer and Ostriker 1973), but the development of spiral arms transports enough mass inward and angular momentum outward so as to stabilize the configuration against fission (Durisen, Gingold, Tohline, and Boss 1986).

References: Chandraskhar, *Ellipsoidal Figures of Equilibrium*. Tassoul, *Theory of Rotating Stars*.

1

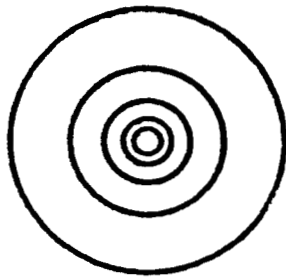$$\int_0^{\pi/2} R(\theta) \sin\theta \, d\theta = 1 + H_o$$

$t = 0$ states

$$P(r,\theta) = \frac{a}{2\pi G r^2} R(\theta) \propto Q$$

Li + Shu (1996)

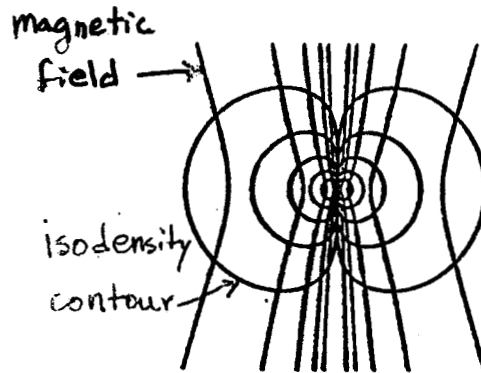$$\Phi(r,\theta) = \frac{4\pi a^2 r}{G^{1/2}} \phi(\theta)$$

- A Linear Sequence of Possible Pivotal Configurations — Toroids!
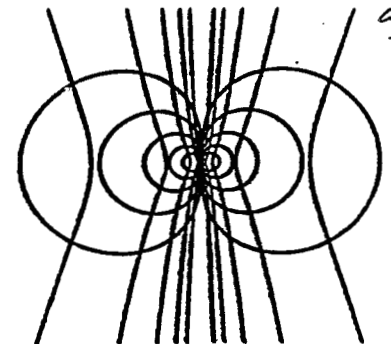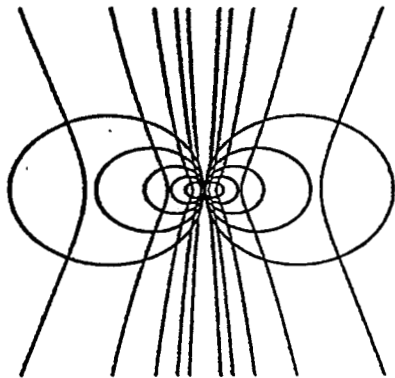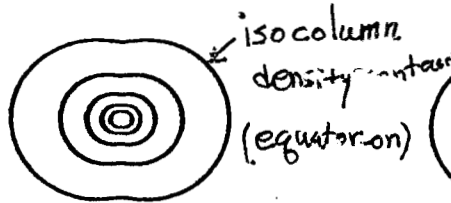
Torrelles e (1981)
Hartmann al. (1

magnetic field →

isodensity contour →

$H_o = 0.0$

$H_o = 0.125$

$H_o = 0.25$

non-magnetized Singular isothermal Sphere

isocolumn density contour (equator-on)

B field

thin disk
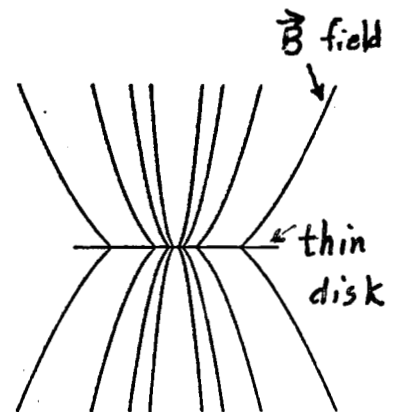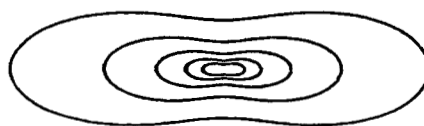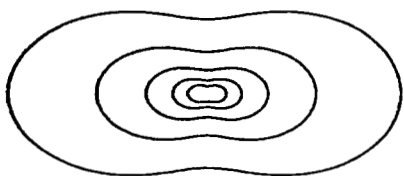
$H_o = 0.5$
$\lambda = 2.66$

$H_o = 1.0$
$\lambda = 1.79$

$H_o \to \infty$
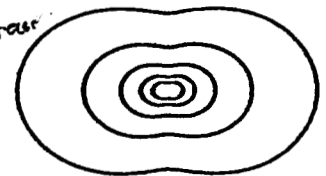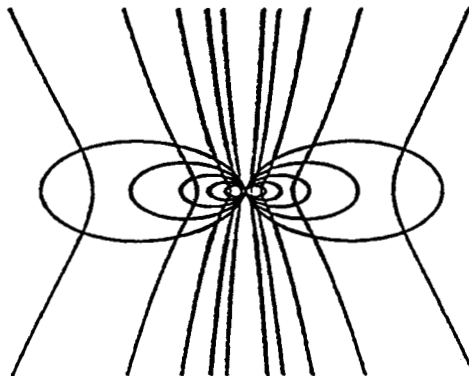
magnetic support only

cf. Myers et al. (1993)

Langer et al. (1996)

on l.1493

cf. Basu + Mouschovias (1994)

Subsequent collapse:
$H_o \ll 1: \dot{M} \approx 0.97$

$H_o \gg 1: \dot{M} = 1.05(1+H_o)$

Theoretical Background

Properties of Molecular Cloud Core :

$\bar{n} \sim 10^4$ cm^{-3} (mostly H_2)

$\bar{T} \sim 10\text{-}30$ K

$\bar{B} \sim 20\text{-}30 \, \mu G$

$n_i/n \sim 10^{-7}$ at $n \sim 10^4$ cm^{-3} (ioniz. by cosmic rays)

$R \sim$ few $\times 10^{17}$ cm or 0.05 pc

$\Omega \sim$ few $\times 10^{-14}$ rad s^{-1}

Properties of Sun :

$\bar{n} \sim 10^{24}$ cm^{-3} (mostly H^+)

$\tilde{T} \sim 10^7$ K

$\bar{B}_{surface} \sim 1$ G ($\gtrsim 10^3$ G in sunspots)

$n_i/n \sim 1$ except in surface layers

$R \sim 10^{11}$ cm

$\Omega \sim$ few $\times 10^{-6}$ rad s^{-1}

Cloud $\rightarrow$ Star : Contraction by few $\times 10^6$ in R and by
10^{20} in $\bar{n}$. Raises two immediate problems

Spin Ang. Mom. Prob. : $R^2 \Omega \sim$ const $\Rightarrow \Omega \uparrow$ by 10^{13} $\otimes$

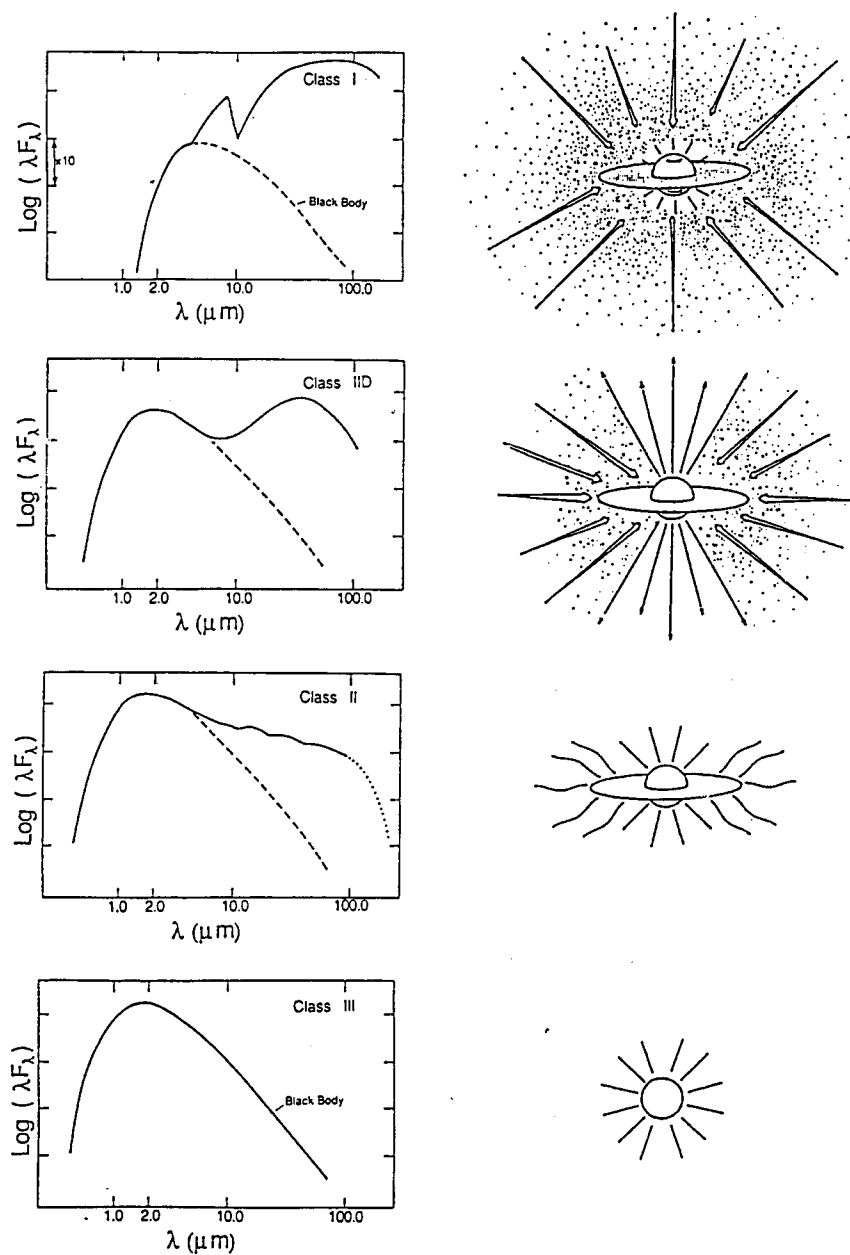Mag. Flux Prob : $R^2 B \sim$ const $\Rightarrow B \uparrow 10^{13}$ $\otimes$

Figure 4.   A schematic of the sequence of protostellar evolution, along with the accompanying evolution of the spectral energy distribution (SED). This figure, taken from Wilking (1989), illustrates the ideas described by Lada (1988a) and in the review article by Shu et al. (1987a).

72   SHU, ADAMS & LIZANO (1987)
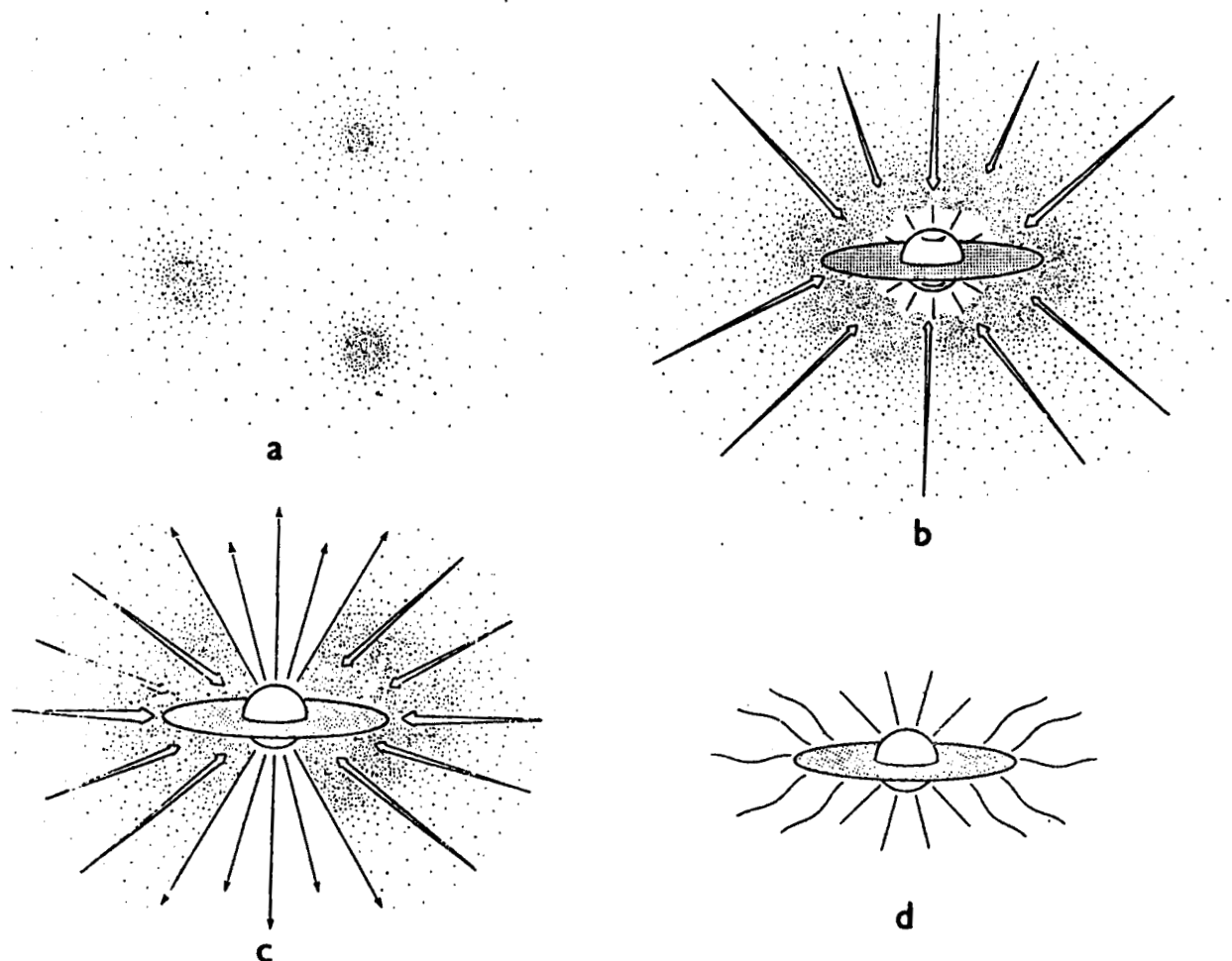
Figure 7   The four stages of star formation. (*a*) Cores form within molecular clouds as magnetic and turbulent support is lost through ambipolar diffusion. (*b*) A protostar with a surrounding nebular disk forms at the center of a cloud core collapsing from inside-out. (*c*) A stellar wind breaks out along the rotational axis of the system, creating a bipolar flow. (*d*) The infall terminates, revealing a newly formed star with a circumstellar disk.

MAGNETIZED SINGULAR ISOTHERMAL DISKS (SIDs)
AND
THEIR BIFURCATIONS

Dimensionless Mass-to-Flux Ratio:

$$\lambda = \frac{2\pi G^{1/2}\Sigma}{B_z} = \text{const} \geq 1.$$

Dilution Factor for Self-Gravity Due to Magnetic Tension:

$$\epsilon = 1 - \frac{1}{\lambda^2}.$$

Enhancement Factor for Gas Pressure Due to Magnetic Pressure:

$$\Theta = \frac{\lambda^2 + 3}{\lambda^2 + 1}.$$

Notice that $\Theta \leq 2$. For unmagnetized SIDs: $\epsilon = 1$ and $\Theta = 1$.

Axisymmetric Singular Isothermal Disk
Surface Density:

$$\Sigma_0(\varpi) = \frac{\Theta a^2}{2\pi G\epsilon G\varpi}\left(1 + D^2\right).$$

Flat Rotation Curve:

$$\Omega(\varpi) = \Theta^{1/2}\frac{D}{\varpi} \qquad \Rightarrow \qquad \text{Epicyclic Frequency}: \ \kappa(\varpi) = 2^{1/2}\Omega(\varpi)$$

Modified Toomre Q:

$$Q \equiv \frac{\Theta^{1/2}a\kappa}{\pi\epsilon G\Sigma_0} = 2\sqrt{2}\frac{D}{(1 + D^2)}.$$

Notice $Q = 1$ for $D = \sqrt{2} \pm 1$, and $Q = Q_{\max} = \sqrt{2}$ at $D = 1$.
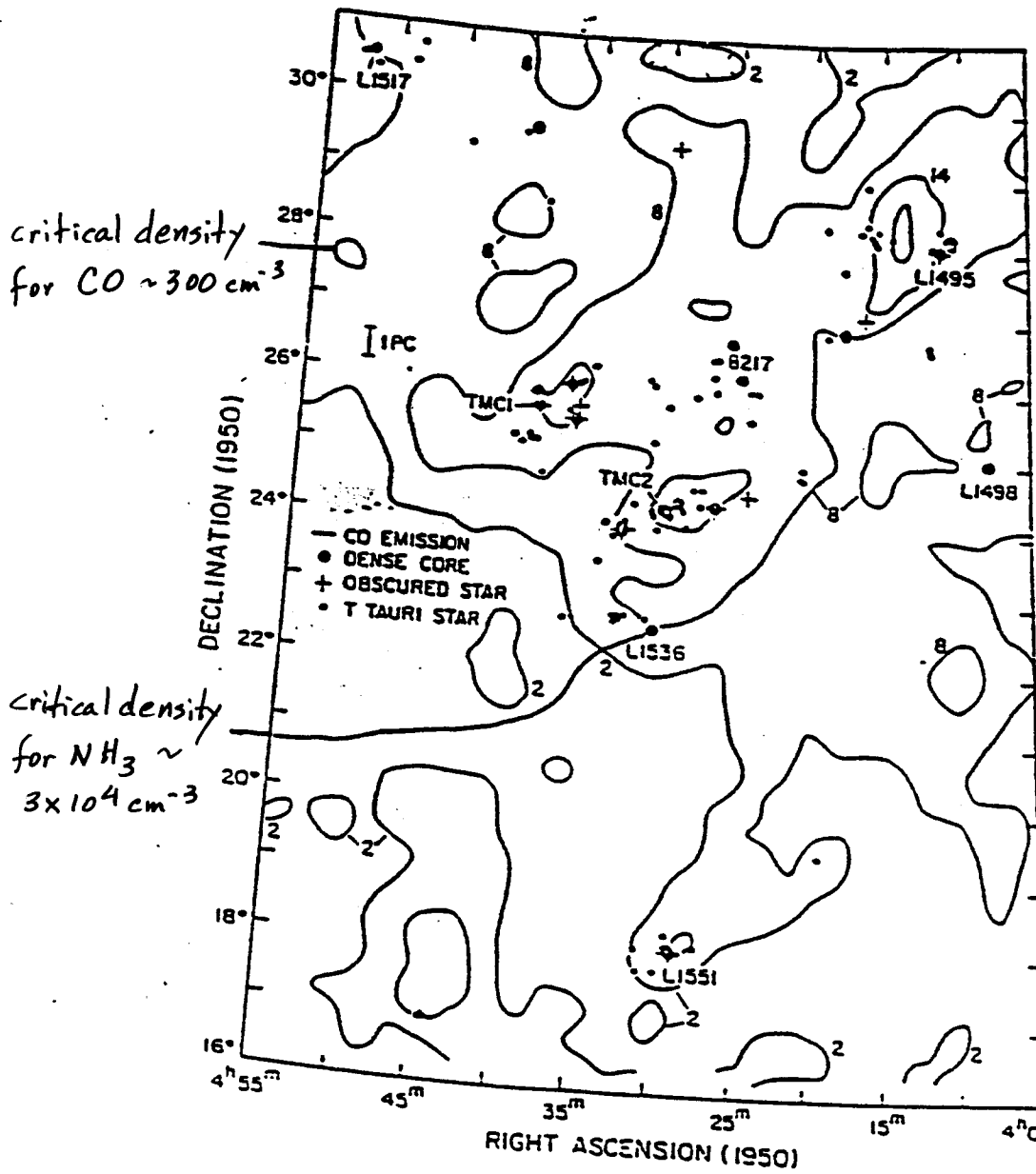
Bifurcations:

$$\Sigma_1(\varpi, \varphi) = \frac{\hat{S}}{\varpi}\cos(m\varphi)$$

have solutions with $\hat{S} \neq 0$ at any D for $|m| = 1$, and at

$$D^2 = \frac{|m|}{|m| + 2} \qquad \text{for} \qquad |m| \geq 2.$$

Analogous to bifurcations of Maclaurin spheroids.

1

Myers (1987)

critical density for CO ~300 cm^{-3}

I 1PC

critical density for NH$_3$ ~ 3×10^4 cm^{-3}

- CO EMISSION
- • DENSE CORE
- + OBSCURED STAR
- • T TAURI STAR

DECLINATION (1950)

30° L1517
28°
26°
24°
22°
20°
18°
16°

RIGHT ASCENSION (1950)
4^{h}55^m 45^m 35^m 25^m 15^m 4^{h}05^m

L1495
B217
TMC1
TMC2
L1498
L1536
L1551

Taurus dark statistics

~50% of den cores conta embedded I

T Tau star ≈ 10 × # der cores seen in NH$_3$ emissio

Since $\langle t_{T Tau} \rangle$ ~ few × 10^6 y

$\langle t_{NH_3 core} \rangle$ few × 10^5 yr

$\langle t_{collapse} \rangle$ 10^5 yr

Time scales are met in picture of molecular cloud core formation by amipolar diffusion (if x_i ~10^{-7} for n~10^4 cm^{-3}, cf. Helmich 1996), followed by inside-out dynamical collapse of isothermal gas at T~10K threaded by fields ~15-20 μG strength at scales ~ 0.1 pc.